Title

A multilayer network model of neuron-astrocyte populations *in vitro* reveals $mGluR_5$ inhibition is protective following traumatic injury

Authors

M.E. Schroeder,[1] D. S. Bassett,[1,2,3,4,5] D. F. Meaney[3,*]

Affiliations

[1]Department of Bioengineering, School of Engineering & Applied Science, University of Pennsylvania, Philadelphia, PA, USA.
[2]Department of Physics & Astronomy, College of Arts & Sciences, University of Pennsylvania, Philadelphia, PA, USA.
[3]Department of Electrical & Systems Engineering, School of Engineering & Applied Science, University of Pennsylvania, Philadelphia, PA, USA.
[4]Department of Neurology, Perelman School of Medicine, University of Pennsylvania, Philadelphia, PA, USA.
[5]Department of Psychiatry, Perelman School of Medicine, University of Pennsylvania, Philadelphia, PA, USA.
*To whom correspondence should be addressed: dmeaney@seas.upenn.edu

Abstract

Despite recent advances in understanding neuron-astrocyte signaling, little is known about astrocytic modulation of neuronal activity at the population level, particularly in disease or following injury. We used high-speed calcium imaging of mixed cortical cultures *in vitro* to determine how population activity changes after disruption of signaling and mechanical injury. We constructed a multilayer network model of neuron-astrocyte connectivity, which captured unique topology and response behavior not evident from analysis of single cell type networks. $mGluR_5$ inhibition decreased neuronal, but not astrocytic, activity and functional connectivity following traumatic injury, and also altered higher-order topological properties of multilayer networks. Comparison of spatial and functional community structure revealed that astrocyte segments of the same cell often belong to separate functional communities based on neural connectivity. Our findings demonstrate the utility of multilayer network models for characterizing the multiscale connectivity of two distinct but functionally dependent cell populations.

41 **Introduction**

42

43 Astrocytes, the most abundant glial cell in the brain, can modulate the activity of neurons
44 through the uptake of neurotransmitters and release of gliotransmitters (*1–5*). One such
45 pathway is uptake of synaptic glutamate through the astrocytic metabotropic glutamatergic
46 receptor subtype 5 ($mGluR_5$) (*6*) (Fig. 1). Through gliotransmission, astrocytes can
47 enhance or depress synaptic plasticity and the synchronization of neuronal circuits (*7-9*).
48 Although less densely expressed in astrocytes than neurons (*10*), $mGluR_5$ has been
49 identified as one of the most prominent receptors implicated in astrocytic detection of
50 neurotransmitters, Ca^{2+} signaling, and downstream synaptic modulation (*1, 5*, *6, 11*).
51 Despite recent advances in understanding neuron-astrocyte signaling, little is known about
52 astrocytic modulation of neuronal population activity, particularly in cases where that
53 activity has been altered by disease and by injury. In this study, we pharmacologically
54 inhibited $mGluR_5$ with the goal of disrupting neuron-astrocyte signaling and elucidating
55 the causal role of astrocytes in modulating neural circuits before and after targeted
56 neuronal injury.

57

58 Based on the large body of evidence supporting a role for astrocytes in establishing
59 neural population synchronization and in protecting against neural degeneration
60 following traumatic brain injury (TBI) (*12, 13*), we hypothesized that astrocytes aid in the
61 recovery of neuronal network synchrony, which is disrupted following moderate
62 mechanical injury to neural tissue (*14*, *15*). To test this hypothesis, we subjected neurons
63 in mixed cultures to targeted injury after $mGluR_5$ inhibition. Previous studies examining
64 astrocyte response to mechanical stretch injury *in vitro* directly triggered injury cascades
65 in astrocytes (*16-18*). In contrast, we examine the interdependence of targeted neuronal

injury and astrocyte activity, enabling us to better isolate the relationship between neuronal injury and neuron-astrocyte signaling. A careful study of neuron-astrocyte communication following injury may reveal mechanisms underlying neural degeneration in TBI and opportunities for therapeutic intervention.

To characterize neuron-astrocyte signaling, we imaged intracellular calcium activity simultaneously in mixed cultures. Moderate speed (> 10 frames per second) imaging of intracellular calcium in individual cells provides a rich data set containing the spatial location and temporal activity of each cell in the population. The emerging field of network neuroscience, which uses tools from graph theory to analyze neural communication as reflected in the topology of interaction patterns, provides an apt set of tools for analyzing multicellular calcium activity. Currently absent, though, is work that links the timing and correlation of calcium transients across different cell types within a mixed cell culture. Multilayer networks are a generalized framework for incorporating multiple types of relations between participating units, capable of describing and modeling a wide range of complex systems (*20-23*). The network formed from bidirectional neuron-astrocyte functional connectivity lends itself to a multilayer network model, where astrocytes and neurons are encoded as nodes in a multilayer network. In analyzing calcium transients that occur across both neurons and astrocytes within the framework of a single network, one can objectively assess the relative influence of one cell type on another, understand whether these cell layers communicate with each other, and identify the role of exogenous factors, such as $mGluR_5$ signaling and traumatic injury, on network structure and function.

The objective of this study was threefold: to determine the spatial and functional topology of neuron-astrocyte networks using a multilayer network model, to characterize changes in topology resulting from single-cell injury and $mGluR_5$ inhibition, and to determine whether fully functional cellular communication is required for post-injury recovery of baseline network topology. We show that pharmacological blockade of mGluR5-mediated neuron-neuron and neuron-astrocyte signaling decreased neuronal network density and altered higher-order topological properties of multilayer networks, including clustering and betweenness centrality. Our results also indicate that $mGluR_5$ inhibition counteracts the topological impact of injury on multilayer networks, or *vice-versa*. More broadly, our findings demonstrate the utility of multilayer network models for characterizing the micro-, meso-, and global-scale connectivity of two morphologically and genetically distinct but functionally dependent cell populations.

Results

We used a multilayer and two single-layer network models to characterize population-level neuron and astrocyte segment dynamics. Neural cell cultures can be modeled as networks without violating the foundational modeling assumptions of network science (*19*). A node represents a single neuron in the neural network, and it represents an astrocyte process in the astrocyte network. Edges are determined by functional connectivity between nodes based on fluorescence activity over time. Each node was assigned to the neuron or astrocyte layer depending on its identity (Fig. 2). In neuron-only networks, each edge representing a functional connection between two neurons was binarized to create an adjacency matrix for each dish (fig. S1); the binarization procedure was implemented to prevent multi-synaptic phase-lagged connections from being analyzed

as direct connections. In astrocyte-only networks and in the multilayer network, each edge representing a functional connection between an astrocyte and a neuron, or between two astrocytes, was weighted by the functional connectivity between them.

The use of weighted matrices for astrocytes and multilayer networks is appropriate because, unlike neuronal calcium events, astrocytic calcium events cannot be binarized. Only cells that were inactive across all conditions were eliminated from the graph, allowing some nodes to have no edges in certain conditions. Dishes were analyzed as separate networks, each with a variable number of nodes. Many useful statistics can be calculated from these graphs, the simplest being the number of nodes and edges. More biologically informative, however, are network parameters describing how cells are functionally connected. Because the plating density of neurons and astrocytes varies between dishes and between isolations, we calculated network measures that can be normalized for network size. Mean degree, density, nodal strength (normalized to network size), clustering coefficient, betweenness centrality (also normalized), and global efficiency (SM sec. A) were calculated for each network and for a random null network model in which both degree distribution and density were preserved. The rationale for reporting these metrics was biologically driven, as they capture general properties of multicellular communication: its overall density, the extent to which connected cells signal to shared neighbors, and the extent to which cells act as hubs, facilitating signaling between other cells. A random null model was chosen because the attachment of cortical neurons and astrocytes to the dish upon plating was random, as was their wiring to other cells after plating.

Effect of $mGluR_5$ blockade and injury on neuron and astrocyte event rates

Next, we sought to determine how experimental manipulations affected functional network topology, which is a higher-order measure of coherent population-level activity. We calculated the mean frequency of calcium events for each cell type in each dish, and then averaged these values over all cells in the field of view that were active at any time point during the experiment. Neuronal event rate decreased following treatment with 2-Methyl-6-(phenylethynyl)pyridine (MPEP), a potent $mGluR_5$ inhibitor, immediately after drug addition but before injury. Following injury, neuronal event rate decreased for the minimum essential media (MEM)-treated group but not for the MPEP-treated group (fig. S2). We used a generalized linear model to quantify the effect of injury, $mGluR_5$ inhibition, and their interaction on neuronal and astrocytic event rates at the final time point. Both $mGluR_5$ blockade and neuronal injury significantly reduced neuronal event rate (a two-sided t-test on linear regression coefficients gave a significant effect of injury (β = -5.086, t = -3.712, p = 0.001) and a significant effect of drug (β = -5.095, t = -3.608, p = 0.001). While the interaction of the two increased activity relative to dishes with either intervention alone (β = 3.672), the effect was not significant (two-sided t-test on linear regression coefficients, t = 1.889, p = 0.068). Astrocytic event rate was unchanged following neuronal injury and $mGluR_5$ inhibition. These results suggest that any changes in functional network topology may be mediated directly through decreased activity in neural layers, while changes in astrocyte layer topology are unlikely to be mediated through decreased astrocyte activity.

Exogenously manipulating neuron network topology

Because glutamate is an important neural and glial transmitter, we targeted $mGluR_5$ to inhibit neuron-to-neuron (N-N) and neuron-to-astrocyte (N-A) communication. We then measured the resulting changes in network topology by calculating the mean degree (K),

density (κ), clustering coefficient (*C*), betweenness centrality (*B*), and global efficiency (*E*) of functional neuronal networks after disruption of $mGluR_5$-mediated N-N and N-A signaling (SM sec. A). Weighted and binary adjacency matrices were generated based on the phase correlation of spikes for each neuron (SM sec. B). For both weighted and unweighted methods, mean degree was positively correlated with mean event rate; for the weighted case we found $R^2 = 0.22$ ($F(1,28) = 7.71$, $p = 0.0097$), and for the binary case we found $R^2 = 0.1891$ ($F(1,28) = 6.53$, $p = 0.0163$). We note that nodes with more spikes and therefore more phases have a higher chance of being correlated with others, and we therefore binarized neuron-only networks. Relative to null networks generated by randomly rewiring connections but preserving degree distribution and density, neuron networks exhibited significantly greater clustering coefficient (Fig. 3A; one-sample t-test on differences between actual values and null model values of *C*, $t = 7.10$, $df = 35$, $p < 0.0001$) and significantly lower global efficiency (one-sample t-test on differences between actual values and null model values of *E*, $t = 6.16$, $df = 35$, $p < 0.0001$). That is, neuron networks have more interconnected triads and fewer long-distance connections, which promote efficiency of communication between nodes, than would be expected based purely on their density.

Administration of the $mGluR_5$ antagonist led to a significant decline in network density after injury (Fig. 3C, Tukey's multiple comparisons test, adjusted $q = 4.70$, $df = 32$, $p = 0.0114$), but not in either injury-only or drug-only groups. We observed a significant effect of time (two-way ANOVA, $F(2,96) = 14.9$, $p < 0.0001$), group assignment (two-way ANOVA, $F(3, 96) = 3.097$, $p = 0.0305$), and the interaction between time and group assignment (two-way ANOVA, $F(6,96) = 2.251$, $p = 0.0447$) on density. Decreased density in MPEP-treated groups was evident at the second time point, where we observed

a significant difference between MPEP/Sham and MEM/Injury groups (Fig. 3D, Tukey's multiple comparisons test, $q = 4.276$, $df = 96$, $p = 0.0166$). This result suggests that fully functional N-N and N-A communication can mitigate the decline in density following injury and may support normal network density at baseline. To test whether changes in topology were mitigated by decreasing network density, we ran a generalized linear regression model (GLM) on the clustering coefficient C, global efficiency E, and mean normalized betweenness centrality B versus group assignment and density. We found that mean density was the greatest, and most statistically significant, covariate of all measures (table S1). The dependence of these topological properties on density is also evidenced by a strong correlation between the density and the clustering coefficient C, the global efficiency E, or the betweenness centrality B (Fig. 3B). Taken together, these results suggest that topological changes of neuronal networks following $mGluR_5$ blockade and injury are largely mediated by changes in local node density.

Spatial embedding and community structure of neuron networks

In addition to functional connectivity, spatial distance between nodes shapes network topology, as neurons that are closer together are more likely to be connected. We sought to test whether physical distance between nodes predicts functional connectivity in our culture system, which can be used to study dynamics in a subset of a larger network. If functional neuronal connections are not spatially restricted, neurons must be able to form relatively long-distance functional connections; then mesoscale topology should change to favor modularity governed by short-distance connections following disruption of neuron-neuron signaling. To test this hypothesis, we compared the community structures predicted by functional and spatial connectivity. The location of each cell in two-dimensional space was extracted from calcium fluorescence recordings. Spatial adjacency

15 matrices were generated such that nodes with the shortest radial distance were most
16 strongly connected. The modularity of both functional and spatial graphs was determined
17 by maximizing the quality function (eq. S14), constructed with a Newman-Girvan null
18 model (*24*), using a Louvain-like locally greedy algorithm implemented in MATLAB
19 (*25*). The spatial tuning parameter was adjusted to minimize the difference between the
20 number of communities in the spatial networks and the number of communities in the
21 functional networks. To compare the modularity predicted by spatial and functional
22 graphs, we calculated the Adjusted Rand Index (*ARI*) (*26*) between the partitions of spatial
23 and functional networks into communities (eq. S18). The Rand Index is equal to one when
24 two community partitions are exactly equal, and zero when there is no overlap. The *ARI*
25 adjusts for the probability of two cells being assigned to the same module by chance and
26 can take on negative values. We found that community structure differed between
27 functional and spatial networks (fig. S3), with the *ARI* between functional and spatial
28 partitions being no different from zero (mean = 0.0021; two-sided one-sample t-test, t =
29 0.3017, df = 35, p = 0.7647). This result suggests that mesoscale functional connectivity
30 between neurons is not dependent on spatial distance in our cultures.
31
32 **Unchanged astrocyte network topology following exogenous manipulation**
33 In general, astrocyte networks were small and sparse. After eliminating segments that
34 were not active at any time during the experiment, only 28 out of 36 dishes remained, with
35 a median of about three active whole cells and about 15 active astrocyte processes per
36 dish. The number of whole astrocytes correlated well with the number of active astrocyte
37 segments, with each active cell having on average around five active segments (fig. S4A).
38 As with neuron networks, we sought to characterize the topology of astrocyte functional
39 networks based on their activity. Weighted adjacency matrices were generated by

calculating the Pearson's correlation coefficient between pairs of filtered and scaled astrocyte calcium traces (SM sec. C). In addition to the network density κ, the global efficiency *E*, the clustering coefficient *C*, the normalized degree *K*, and the normalized betweenness centrality *B*, we calculated the mean nodal strength (*S*) of each astrocyte network and normalized it for network's size. To test whether these network statistics were topologically meaningful (non-random) after controlling for network size and density, we compared them to those of a null model in which connections were randomly rewired while preserving the degree distribution and density. Similar to the neuron networks, functional astrocyte networks displayed significantly higher clustering coefficient (one-sample t-test on differences between the actual values and null model values of *C*, $t = 3.692$, $df = 22$, $p = 0.0016$) and significantly lower global efficiency (one-sample t-test on differences between actual values and null model values of *E*, $t = 4.450$, $df = 22$, $p = 0.0002$) than control networks (fig. S4C).

We observed no significant difference in density or mean strength of astrocyte networks after treatment with anti-$mGluR_5$ or after injury. Similar to controlling for density in neuronal networks, we controlled for mean nodal strength in astrocyte networks to isolate the effect of our manipulations. We found that the clustering coefficient *C*, betweenness centrality *B*, and global efficiency *E* were strongly correlated with density (fig. S4B). Regressing out strength using a GLM eliminated significant effects of group assignment on all measures, except for the effect of injury on betweenness centrality (table S2, $\beta = 0.471$, two-sided t-test on regression coefficient, $t = 2.440$, $p = 0.026$). Interestingly, in contrast to the neuronal networks, the betweenness centrality *B* of the astrocyte network was inversely correlated with density (linear regression, slope = -1.151 ± 0.2710, $F(1,21) = 18.03$, $p = 0.0004$). Although the centrality of nodes usually increases with strength in

weighted random graphs, this may not be true for extremely small and sparse networks with non-random topology in which a single node has a high likelihood of becoming a hub. In fact, astrocyte segment betweenness centrality *B* was lower, though not significantly, than that of control networks, while it was relatively higher for neuron networks. Thus, astrocyte segments have lower-than-expected betweenness centrality, and less hub character, than would be expected from their average connection strength. From a biological standpoint, it is reasonable that fewer astrocyte segments dominate astrocyte networks as hubs, since microdomains are thought to respond to local activity.

Exogenously manipulating multilayer network topology

While it is useful to consider neuron and astrocyte networks separately, neurons and astrocytes do not exist in isolation. To better understand the interactions between neurons and astrocytes, and to assess whether the topology of these sub-populations is independent of or informed by the other, we modeled neuron-astrocyte functional interactions as a multilayer network (Fig. 2, Fig. 4A-C). As for astrocyte networks, edges for multilayer adjacency matrices were assigned weights from the functional connectivity between neurons and neurons, between astrocytes and astrocytes, and between neurons and astrocytes, as measured by the Pearson's correlation coefficient of filtered and scaled calcium traces (SM sec. C). Strength and density were calculated for the entire multilayer network, for neuron and astrocyte layers separately, and for interlayer connections separately. Mean normalized betweenness centrality, mean clustering coefficient, and global efficiency were calculated for the entire multilayer network, for each layer, and for control networks generated as previously described.

Consistent with our findings for neuron and astrocyte networks individually, multilayer networks exhibit significantly larger clustering coefficient C (one-sample t-test on differences between actual values and null model values, $t = 6.033$, $df = 26$, $p < 0.0001$) and lower global efficiency E (one-sample t-test on differences between actual and null, $t = 12.19$, $df = 26$, $p < 0.0001$) than their randomized counterparts (Fig. 4E); no differences in betweenness centrality B were observed. Nodal strength in the neuron network layer (one-sample t-test on differences between actual values and null model values of S, $t = 2.995$, $df = 26$, $p = 0.0060$) and in the astrocyte network layer (one-sample t-test on differences between actual values and null model values of S, $t = 3.569$, $df = 26$, $p = 0.0014$) was higher than expected in randomized multilayer networks that preserved strength. Interestingly, mean nodal strength calculated only from interlayer edges was lower than that expected in randomized controls (Fig. 4D, one-sample t-test on differences between actual values and null model values of S, $t = 2.716$, $df = 26$, $p = 0.0116$). Further, the astrocyte layer nodal strength was significantly larger than that of the neuron layer (Holm-Sidak multiple comparisons test, $q = 5.264$, $df = 104$, $p = 0.0018$) and than that of interlayer edges (Holm-Sidak multiple comparisons test, $q = 8.863$, $df = 104$, $p < 0.0001$); the astrocyte layer nodal strength was also significantly larger than the nodal strength in the entire multilayer network. In other words, intralayer connections are stronger than interlayer connections, and astrocyte segments are more strongly interconnected than neurons, compared to random networks maintaining the same mean nodal strength.

To assess the impact of $mGluR_5$ inhibition, injury, and their interaction on multilayer network topology, we fit a GLM to multilayer graph statistics including the betweenness centrality B, the clustering coefficient C, and the global efficiency E. The outcome variable of interest was calculated for each dish at the third time point and regressed on its

group assignment while controlling for mean nodal strength as a covariate of non-interest. Notably, while network measures also correlated with density in multilayer networks (Fig. 4E), the treatment condition still accounted for a significant amount of their variation at the final time point (table S3). After controlling for strength in this manner, $mGluR_5$ blockade, injury, and their interaction significantly altered network topology. Following injury, we observed a significant increase in the betweenness centrality B (two-sided t-test on estimated coefficients, $\beta = 0.310$, $t = 4.30$, $df = 22$, $p = 0.0003$) and in the clustering coefficient C (two-sided t-test on estimated coefficients, $\beta = 0.035$, $t = 2.22$, $df = 22$, $p = 0.037$), but no change in the global efficiency E. After $mGluR_5$ blockade, we observed an increase in the betweenness centrality B (two- sided t-test on estimated coefficients, $\beta = 0.237$, $t = 3.24$, $df = 22$, $p = 0.004$) but no change in the clustering coefficient or global efficiency. In contrast, after both injury and $mGluR_5$ inhibition, we observed a decrease in the betweenness centrality B (two-sided t-test on estimated coefficients, $\beta = -0.447$, $t = -4.54$, $df = 22$, $p = 0.0002$). Collectively, these results suggest that that $mGluR_5$ inhibition and mechanical trauma produce counter effects on topology. Further, while both manipulations affected betweenness centrality, only injury impacted the clustering coefficient. Moreover, changes in clustering, controlled by mean nodal strength, were only evident when neuron and astrocyte layers were analyzed together in a multilayer network, and not when the layers were studied separately.

To control for the effect of using weighted edges in the neuron layer of the multilayer network in contrast to using binary edges in the single-layer neuron network, we repeated the above procedure using weighted edges for the neuron networks, generated using the same procedure as for the astrocyte and multilayer adjacency matrices (SM sec. D). Inclusion of the astrocyte layer and interlayer connections improved the fit of the

generalized linear model predicting network properties from treatment condition relative to a model of either layer alone. Treatment induced changes in the betweenness centrality *B* were significantly predicted in the weighted neuron networks (table S4), though to a lesser degree. This result indicates that multilayer changes in the betweenness centrality *B* are mostly mediated by changes in the neuronal layer, while changes in the clustering coefficient *C* are mediated by changes in both layers and in the connections between layers. Additionally, to measure the impact of the relative abundance of neurons to astrocytes on multilayer topology, we sub-sampled the neuron population to equal the number of astrocytes and recalculated network statistics on these synthetic half-neuron, half-astrocyte networks (SM sec. E). Sub-sampled multilayer networks exhibited similar baseline topology, but slightly different response behavior, than full multilayer networks, suggesting that the relative abundance of neurons partially drives changes in topology.

Spatial embedding of and community structure in astrocyte and multilayer networks

In addition to local and global topological statistics, we sought to understand the community structure, or modularity, of multilayer neuron-astrocyte networks and astrocyte layers. While spatial distance between two nodes in the same layer might not predict their functional community membership, we asked if the multilayer modularity, determined using information about interlayer functional connectivity, more closely matches spatial modularity (Fig. 5A-D). In other words, is the strength of functional connections between neurons and astrocyte segments related to spatial proximity at the ~1mm scale? To address these questions, we compared the community structures predicted by functional and spatial connectivity in astrocyte and multilayer networks using the same methodology as for neuron networks.

To test whether functionally-predicted modularity matched structurally-predicted modularity, we computed the *ARI* between functional and actual multilayer communities. The mean *ARI* between spatial and functional multilayer communities was near but significantly greater than zero (mean = 0.0536, one sample t-test, $t = 4.395$, $df = 22$, $p = 0.0002$). This disagreement between spatial and functional partitioning was not driven by differences in community size, as γ, the spatial tuning parameter, was adjusted to minimize this difference (Fig. 5E, $\gamma_s = 1.13, \gamma_f = 1.55$; paired t-test, $t = 0.1645$, $df = 22$, $p = 0.8709$). This finding suggests that functional connectivity of neurons and astrocytes is largely independent of distance at this scale *in vitro*. Furthermore, the choice to use the multilayer modularity approach allowed us to calculate cell type specific participation across modules (Fig. 5F). Relative to astrocyte segments, neurons participated in a greater fraction of functional (Tukey's multiple comparisons test, $q = 8.549$, $df = 88$, $p < 0.0001$) and spatial (Tukey's multiple comparisons test, $q = 11.28$, $df = 88$, $p < 0.0001$). This difference in module participation reflects the dominance of neurons in quantity, as sub-sampled networks with an equal number of neurons and astrocytes had near equal spatial and functional participation of both cell types (SM sec. E).

Because astrocytes were subdivided into smaller functional units of microdomains, their functional modularity could be directly compared to their morphological (actual) modularity, which serves to group segments of the same cell. This approach enabled us to test whether microdomains of the same astrocyte are functionally independent at the mesoscale. To test whether functional and spatial graphs of astrocyte segments matched actual cell morphology, we computed the *ARI* between functional, spatial, and actual astrocyte communities. Astrocyte microdomains were manually grouped into whole cells based on maximum fluorescence projection images. Community partitions between the

three graph types (functional, spatial, and actual) were different, with ARI < 0.4 for all (Fig. 6). Interestingly, the *ARI* between cellular and functional communities was largest, significantly larger than cellular versus spatial (Tukey's multiple comparisons test, q = 3.369, df = 132, p = 0.0486) and spatial versus functional (Tukey's multiple comparisons test, q = 4.531, df = 132, p = 0.0048) community partitions generated from multilayer networks. Differences in community membership were not predominantly attributable to changes in community size or community number between graph types, as γ was tuned to minimize differences in mean community size of the three partitions at baseline ($\gamma_s = 1.15, \gamma_f = 1.51$, one-way ANOVA, $F(2,66) = 0.08331$, $p = 0.9202$). Differences in actual, spatial, and functional modularity suggest that astrocyte segments behave relatively independently from the rest of the cell and tend to co-function with neurons.

When multi- and single-layer astrocyte *ARI*'s were grouped, differences between module types were significant (two-way ANOVA comparing the effect of module type and single or multilayer network on *ARI*: $F(1,132) = 7.675$, $p = 0.0062$). This finding highlights the functional independence of astrocyte segments of the same cell in both their own layer and in the multilayer network. Further, *ARI* between all module types was improved when astrocyte communities were assigned from multilayer graphs, although this improvement was not statistically significant (two-way ANOVA comparing the effect of single versus multilayer network type on *ARI*, $F(2,132) = 5.840$, $p = 0.0037$). That is, incorporating information about neural activity improved the agreement between morphologically and functionally determined astrocyte segment modules. One interpretation of this finding is that functional connectivity between astrocyte segments and neurons is more influenced by spatial proximity than is functional connectivity between astrocyte segments. Furthermore, this improvement in morphology-function agreement in multilayer astrocyte

communities, which include neurons, suggests that the two populations are not functionally independent. If they were independent, we would expect the community structure of astrocyte segments to remain unchanged after multilayer modularity analysis.

Immunofluorescent localization of mGluR$_5$ on neurons and astrocytes in culture

To verify the presence and assess the relative abundance of mGluR$_5$ on neurons and astrocytes in our cultures, we stained for mGluR$_5$; microtubule associated protein 2 (MAP2), a neuronal marker; glial fibrillary acidic protein (GFAP), an astrocytic marker; and nuclei (Hoechst stain), for counting purposes. Six dishes of naïve cells were fixed at DIV 10, the same age at which experimental cells were treated and imaged, stained using immunofluorescent antibodies (SM sec. F), and imaged in three fields of view. MAP2 and mGluR5 colocalized in 99% of neurons (n = 6 dishes, n = 3 fields of view each, n = 525 neurons total), verifying expression of the receptor on neurons. GFAP and mGluR$_5$ colocalized in 76% of astrocytes (n = 6 dishes, n = 3 fields of view each, n = 119 astrocytes total), confirming the expression of the receptor in astrocytes. However, anti-mGluR$_5$ intensity was visibly lower in astrocytes than in neurons (fig. S5), suggesting that neurons in our cultures express more mGluR$_5$ than astrocytes. A notable limitation of GFAP as an astrocyte marker is that it does not stain fine astrocyte processes or microdomains (*27*), where mGluR$_5$ is more likely to be located (*4, 5*). Thus, our stain may not have captured the full extent of astrocytic mGluR$_5$ expression.

Discussion

Using an *in vitro* model of traumatic brain injury, this study examined the functional response of cultured neuron-astrocyte populations to disruption of mGluR5-mediated

signaling and mechanical injury. A multilayer network model of neuron- astrocyte connectivity captured unique topology and response behavior not evident from networks of one cell type. $mGluR_5$ inhibition decreased neuronal, but not astrocytic, activity and functional connectivity following injury, and altered higher-order topological properties of multilayer networks, including the clustering coefficient and betweenness centrality. In order to determine whether network connectivity between cells was primarily determined by spatial proximity, we compared the community structure of networks generated using calcium activity and spatial location. This analysis revealed that functional connectivity is independent of spatial proximity in small-scale *in vitro* neuron-astrocyte networks. Interestingly, we observed that segments of the same astrocyte often interact with separate functionally connected communities of neurons. Taken together, our results suggest that while astrocytes and neurons are functionally connected, $mGluR_5$ is not the primary receptor mediating neuron-astrocyte communication in our culture system. In this discussion, we explore potential explanations for our findings and their significance in the context of glial biology and traumatic brain injury.

Disrupted neuronal functional connectivity following mechanical injury and $mGluR_5$ blockade

Previous studies using other *in vitro* models have shown that mechanical injury to neurons reduces functional connectivity (*13-15*). In line with these studies, our results show that single-cell tap injury to multiple neurons reduces overall network connectivity, likely because injury leads to functional uncoupling of a neuron and its neighbors. Consistent with these studies, our results show that mechanically injuring a fraction of neurons in the network reduces overall network connectivity, likely because injury leads to a functional uncoupling of a neuron with its neighbors. At a mechanistic scale, the reduction in

connectivity could occur simply from the reduction in network density that occurs when neurons are mechanically ablated from the microcircuit. In addition, it is possible that local mechanical trauma can lead to a release of neurotransmitters from the injured neuron that will inhibit local neurotransmission. Past work studying neuron-astrocyte coupling after mechanical trauma points to the role of ATP release and activation of purinergic receptors as key for mediating a spreading wave in neuronal inactivation that can coincide with intracellular calcium waves from the injured area (*28*). Regardless of its exact origin, our results demonstrate the intricate interruption in balance across neuronal and astrocyte layers that occurs from microtrauma to neuron-glia networks.

Our observation showing that network density decreased further following $mGluR_5$ inhibition suggests that glutamate signaling via this receptor promotes and restores density in neuronal networks. This finding is in agreement with previous work, which has found that long-term potentiation (LTP) at thalamic input synapses was impaired following bath application of MPEP *in vitro* (*29*). In *in vivo* follow-up, administration of MPEP dose-dependently impaired the acquisition of auditory and contextual fear learning, implicating $mGluR_5$ in neuronal plasticity, and highlighting the functional importance of this receptor. In another study, $mGluR_5$-deficient mutant mice showed a complete loss of the NMDA-receptor mediated component of LTP in hippocampal CA1 neurons (*30*). From these and our results, we infer that $mGluR_5$ plays an important role in establishing and maintaining the functional connectivity of neural circuits.

Unchanged neuron-astrocyte connectivity following $mGluR_5$ inhibition

While molecular and cellular changes following direct injury to astrocytes is well-documented (*16-18*), the functional contribution of astrocytes to neural population activity

in response to targeted neuronal injury is unknown. Due to the expression of $mGluR_5$ on neurons and astrocytes, we were unable to target astrocyte-specific $mGluR_5$ pharmacologically. Thus, we could not determine whether changes in neuronal network density were attributable to changes in gliotransmission. Contrary to our initial hypothesis, astrocyte activity and functional connectivity did not decrease following injury or $mGluR_5$ inhibition. Because we did not directly injure astrocytes, their lack of direct response to injury after one hour is perhaps expected.

However, the lack of astrocyte response to $mGluR_5$ blockade is more difficult to interpret. It could be that astrocytes are able to compensate for impaired glutamatergic signaling through other modes of intra-astrocyte communication, including gap junctions and other biochemical receptor pathways. Alternatively, we may have examined astrocyte activity at too course of a spatial scale. Astrocyte mGluRs are localized in microdomains, which we were unable to visualize under cytosolic GCaMP6f or GFAP staining. Thus, we likely did not observe the full extent of astrocyte activity and its dynamics following injury and $mGluR_5$ inhibition. Improper spatial resolution might also explain the low expression of $mGluR_5$ on astrocytes relative to neurons observed in stained cultures. Additionally, previous work indicating a critical role for $mGluR_5$-mediated neuron-astrocyte communication was primarily conducted in slices and *in vivo*, rather than in dissociated cultures. Thus, it is possible that different gliotransmission pathways, perhaps purinergic (*6*), are relatively more important in our cultures, which differ in age, health, cellular composition, and genetic variation from astrocytes in slices and *in vivo*.

Protective effect of pre-injury $mGluR_5$ blockade on multilayer network topology

While $mGluR_5$ inhibition did not alter astrocyte population activity, it did change the topology of multilayer networks, an effect that was not observed completely in neuron or astrocyte populations alone. Analysis of weighted neural graphs revealed a significant effect of $mGluR_5$ inhibition, injury, and their interaction on betweenness centrality, after controlling for mean connection strength. Inclusion of the astrocyte layer and interlayer connections revealed treatment- and injury-driven changes in clustering coefficient, as well as improved estimates of treatment effects on betweenness centrality. Significant treatment-driven changes in clustering were not observed in either the neuron or astrocyte single-layer model. Taken together, these results suggest that multilayer changes in betweenness centrality are mostly mediated by the neuronal layer, while changes in clustering and efficiency are mediated by changes in both layers and the connections between them.

Injury increased the clustering coefficient, reflective of closure in local neighborhoods, and the mean betweenness centrality, reflective of transmission bottlenecks, in the multi-layer network. $mGluR_5$ inhibition also increased betweenness centrality. These topological changes may result from functionally eliminating nodes through which long-distance paths pass, forcing more of the remaining healthy neuronal nodes to adopt hub roles, thereby increasing local clustering. The interaction of injury and drug had the opposite effect on clustering and betweenness centrality, suggesting either that $mGluR_5$ inhibition prevents the impact of injury on topology, or that injury reverses the impact of $mGluR_5$ blockade. This protective effect of $mGluR_5$ inhibition following injury was observed in previous studies *in vitro* and *in vivo* (*31, 32*), and has been attributed to a reduction in NMDAR activity following $mGluR_5$ inactivation.

Independence of spatially and functionally predicted communities in small-scale neuron-astrocyte networks

Functionally and structurally informed modularity of *in vitro* neuronal networks has not been explored. Because cultured cells exist in a constrained 2-dimensional environment, devoid of connective tissue and vasculature, the spatial organization of *in vitro* networks is likely to be different from that of *in vivo* networks. Furthermore, we examined a small subsection of a larger network in this study. In this context, it is logical that the functional and spatial community structure of neuron-astrocyte networks is independent. Neurons and astrocytes can connect with one another over distances an order of magnitude larger than the ~1mm field of view imaged in this study. Thus, functional connectivity can be established independent of spatial proximity. It could be that spatial proximity only influences functional modularity at and above a certain scale.

That astrocyte segments form functional modules independent of morphological and spatial communities reflects the functional independence and heterogeneity of astrocyte calcium events (*33*). If segments of the same astrocyte participate in different functional modules, there is likely a functional advantage to maintaining strong inter-astrocyte and astrocyte-neuron connectivity above intra-astrocyte connectivity. This microdomain independence allows a given astrocyte to sense and integrate activity from a diverse set of neurons over time and space (*34, 35*). Multilayer astrocyte modularity recapitulated this mesoscale structure-function independence, but to a lesser degree. Taken together, the results of our multilayer network analysis provide topological evidence that neuron and astrocyte populations are functionally interdependent.

Methodological considerations

A major limitation of this study is the extreme sparseness of active astrocyte segments relative to neurons in our cell cultures. Neuronal dominance of multilayer network dynamics likely skewed multilayer topology towards the neuronal layer. The low level of activity in astrocytes could be due to our examination of astrocyte activity at specific spatial and temporal scales or to the health of the cells in culture. Prior work indicating critical roles for neuron-astrocyte communication in plasticity, synchronization, and behavior, were primarily conducted in slices and *in vivo*, and many involved direct stimulation of neurons or promoted arousal to evoke an astrocyte response (*10*). In contrast, we examined relatively asynchronous spontaneous neural activity in dissociated cultures. The astrocytes in our model system may not have developed the complete range of neuromodulatory activities performed by those *in vivo*.

The interpretation of our findings depends on relative $mGluR_5$ expression and signaling importance in the neurons and astrocytes in our cultures. The presence and importance of $mGluR_5$ on neurons and in their signaling is well-documented and has been confirmed with immunofluorescent staining of $mGluR_5$ in our *in vitro* preparations. Indeed, the decrease in neuronal network density following MPEP administration is likely attributable to blockade of neuron-neuron communication. This is an inherent limitation in conventional pharmacological studies of gliotransmission. To isolate the causal effect of astrocyte-specific signaling on neural circuit activity, future experiments could use more sophisticated tools such as designer receptors exclusively activated by designer drugs (DREADDs), astrocyte-specific G-protein coupled receptor opsins (*36*), or genetic knockdown.

Another potential weakness of this study is the use of binary adjacency matrices for neurons and weighted matrices for astrocytes. Binarization of neuronal connections likely reduces the number of phase-lagged multi-synaptic connections interpreted as direct connections (SM sec. G). Because astrocytic calcium events cannot be binarized like neuronal ones, weighted matrices are more appropriate for astrocyte and multilayer networks. While it is likely that two neurons will have phase-locked calcium events, it is highly unlikely that the calcium activity of two astrocyte segments will be exactly matched at any point in time. Thus, it would be arbitrary to assign binary connectivity to astrocytes. To control for the effect of using binary neural networks on our significant findings, we fit a generalized linear model to experimental data using weighted neural graphs and found that the most significant results still hold.

Future directions: *in vivo* and expanded models of neuron-glia networks

The aforementioned differences in health and activity between astrocytes *in vitro* and *in vivo* motivate future work comparing the topology and response behavior of neuron-astrocyte networks in cell culture and animal models. Assuming that the number of active astrocyte microdomains *in vivo* is greater than in culture, we speculate that there would be significant changes in neuron-astrocyte network community structure, as astrocytic participation in spatial and functional models would increase. Similarly, we speculate that there is increased density and strength of astrocyte-astrocyte and neuron-astrocyte connections *in vivo*. Given our findings that betweenness centrality, global efficiency, and clustering are mostly influenced by density and strength, these topological properties would change accordingly in *in vivo* networks. Furthermore, with greater neuron-astrocyte connectivity *in vivo*, neuronal manipulations, such as injury, would induce a greater change in multilayer and astrocyte layer network topology. Additionally, we propose that

the topology of neuron-astrocyte networks changes from its spontaneous state during periods of intense stimulation, given that astrocytes exhibit unique responses to stimulation and during behavior (*10, 37, 38*). For example, there may be increased alignment between morphological and functional astrocyte communities during stimulation, as repeated neuronal firing triggers global astrocyte Ca^{2+} events (*39*). It is difficult to speculate how our findings related to $mGluR_5$ inhibition will translate *in vivo*, as the relevance of $mGluR_5$-mediated gliotransmission in adult rats is debated (*40*).

The field of network neuroscience was largely built upon observations of structural connectivity at the whole brain or macroscale represented as graphs (*19*). Combined with the ever increasing focus on data science, the field has left first-principles descriptions of functional connectivity at the elementary (single-neuron) level relatively underexplored. Our work aids in addressing this understudied area by characterizing the topology, and changes therein, of functional connections between elementary-scale mixed cortical cultures. Further, to our knowledge, the field is devoid of any models describing or predicting connectivity between neurons and glia, although there are some computational neuroscience models that explore the interactions of these two cell types. Network modeling of neuron-glia interactions is an area ripe for future study and is particularly well suited for characterization and prediction using multilayer models.

Multilayer networks have been used to model brain network development over time, to compare healthy and diseased brains, to predict structure–function relationships, and to link multiscale and multimodal data (*22*). Despite the increasing popularity of multilayer networks and the existence of multiple neural cell types, there has been limited use of the multilayer framework to study interactions between two or more cell populations. Here,

we demonstrate the validity of a multilayer network model to characterize the connectivity of neuron-astrocyte populations. Multilayer neuron-astrocyte networks maintain unique topology from their individual layer components. Further, the multilayer model captured topological effects of experimental manipulations not evident from independent analysis of the individual layers. That is, incorporating the connectivity of astrocytes and neurons was necessary to reveal changes in network topology.

Conclusion

Our results indicate that $mGluR_5$ is not essential for maintaining spontaneous astrocyte-astrocyte or neuron-astrocyte functional connectivity in non-injured cultures. However, $mGluR_5$ blockade partially restored baseline topology of multilayer networks following traumatic injury, underscoring the potential therapeutic benefit of modulating glutamatergic tone. More broadly, we have proposed and demonstrated the utility of a multilayer network model of *in vitro* neuron-astrocyte populations in interpreting the topological impacts of various experimental manipulations. Our findings support the notion that neurons and astrocytes are not functionally distinct populations, but rather display an interdependent topology that reveals network responses not observed in either population alone. Future work could aim to isolate the astrocytic contribution to static and dynamic network topology using more targeted experimental manipulations, and could study healthy neuron-astrocyte populations *in vivo*, where astrocytes may be more abundant and active.

Materials and Methods

Experimental Design

All animal procedures were approved by the University of Pennsylvania Institutional Animal Care and User Committee. Timed pregnant Sprague-Dawley rats were anesthetized with 5% CO_2 and sacrificed via cervical dislocation. Embryos at day E18 were surgically removed and their neocortical tissue dissected and dissociated for 15min at 37°C in trypsin and DNAse. Following trituration and filtration through Nitex mesh, cells were resuspended in minimum essential media (MEM) with Earl's salts and GlutaMAX supplemented with 0.6% D-glucose, 1% Pen-Strep, and 10% Horse Serum. Cells were plated on glass-bottomed Matteck dishes coated in poly-D-lysine and laminin at a density of 300,000 cells/mL. Cultures were grown in a humidified incubator at 37°C and 5% CO_2, maintained in serum-free MEM and 0.2% Gluta-MAX (Gibco), and fed twice weekly with 1X NEUROBASAL medium (ThermoFisher).

To visualize the calcium activity of astrocytes in addition to neurons, cells were transduced using Adeno-associated virus Serotype 1 (AAV1) carrying the gene for GCaMP6f under a CAG promoter, which is general to mammalian cells (AAV1.CAG.Flex.GCaMP6f.WPRE.SV40, Addgene), at DIV3. Dishes were randomly chosen to be treated with 1uM 2- Methyl-6-(phenylethynyl)pyridine (MPEP), a potent $mGluR_5$ inhibitor (n = 19), or MEM only (n = 36 total). Calcium images were obtained at 488nm excitation, 50ms exposure on a Nikon Eclipse TE2000 confocal microscope. Eight to nine dishes in each treatment group were mechanically injured by briefly deforming the cell surface with a vertical movement of a pulled glass micropipette tip. The micropipette was controlled manually with a microcontroller (Eppendorf), directly perturbing the cell with the pipette tip. Care was taken to avoid rupturing the cell membrane, which would have caused immediate cell death. This model enabled precise, controlled injury of a similar severity across dishes.

Image processing

Images were manually segmented to identify neurons and astrocyte segments as regions of interest (ROIs). Neuronal and astrocytic fluorescence traces were extracted from each ROI as pixel brightness over time (fig. S6). Neuronal and astrocytic events were identified automatically using a custom-built MATLAB template-matching algorithm (SM sec. G), based on the trace's correlation with a library of true neuron and astrocyte calcium waveforms. Automatically identified events were manually confirmed based on calcium traces or eliminated following event detection. Because astrocytic activity was mostly localized to processes that often fluoresced independently, astrocyte segments were analyzed as separate entities. Cells predicted to be astrocytes based on morphology were confirmed based on their functional response to 100uM NMDA administered with 1uM of glycine co-agonist (SM sec. H). Only ROIs that had one or more confirmed calcium events in one or more recordings were kept for further analysis. This pruning step eliminated a significant number of nonactive astrocyte segments, reducing the number of dishes with two or more active astrocyte segments to 23 from 36.

Generation of adjacency matrices

Adjacency matrices for neuron-only networks were generated using a previously described method for determining functional connectivity of *in vitro* calcium activity of rat cortical neurons (*14*). Briefly, the spike times t_i of each neuron i were used to generate a time-varying instantaneous phase $\varphi_i(t,n)$ to each neuron in each inter-spike interval. The instantaneous phase differences between each pair of neurons was calculated as described in SM sec. B. Functional connectivity was binarized by comparing actual phase difference $\psi_{x,y}(t)$ to that of surrogate time series with the same marginal distribution and power

spectrum, generated using an amplitude adjusted Fourier transform (AAFT) algorithm (*41*). Only pairs of neurons that had a phase difference significantly larger or smaller than the surrogates, according to a Kolmogorov-Smirnov test with $p < 0.001$ and $\alpha = 0.05$, were linked with an edge having a weight of unity.

Because astrocytes are not electrically active and do not spike as neurons do, converting astrocyte calcium activity to binary event trains is not appropriate. Thus, we based astrocytic functional connectivity on filtered, scaled calcium fluorescence. For a pair of ROIs, we calculated the Pearson's correlation coefficient between their filtered, scaled calcium fluorescence traces and between each trace and 100 surrogates with similar properties to the original traces. Only node pairs whose correlation was significantly different from that of the surrogates were assigned an edge with a weight equal to their correlation coefficient (SM sec. C). Multilayer adjacency matrices were generated by calculating the pairwise Pearson's correlation coefficient between all cells in the field of view, as described in the previous section. Adjacency matrices were organized as shown in Fig. 2, with neuron-neuron, neuron-astrocyte, and astrocyte-astrocyte adjacency matrices concatenated. Spatial adjacency matrices were generated by measuring the radial distance between the center of each region of interest (ROI) of each node pair, (x_1,y_1) and (x_2,y_2), as $\sqrt{|(x2-x1)|^2 + |(y2-y1)|^2}$. The distance was normalized to the maximum possible distance in the field of view and subtracted from one so that the pairs of nodes with the shortest radial distance were linked by edges with the highest weights. Null networks were generated by randomizing adjacency matrices while preserving degree distribution and density using the *randmio* function in the BCT (*42*). Edges in networks with more than three edges were rewired 100 times for neuron networks, 10 times for astrocyte networks due to their smaller size, and 100 times for multilayer networks.

Calculation of network statistics

Density, strength, clustering coefficient (*C*), betweenness centrality (*B*), and global efficiency (*E*) were calculated for neuron, astrocyte, and multilayer networks using weighted or unweighted definitions as appropriate. Equations are provided in the SM sec. A. In most cases, MATLAB scripts from the BCT were used for calculations (*43*). The form of the multilayer adjacency matrices lends itself to straightforward calculation of network statistics in the same way as for single-layer networks. To compare the topology of the two layers and intra- vs. inter-layer connections, we calculated mean nodal strength of the entire network, mean nodal strength of each individual layer, and mean strength of interlayer connections. Interlayer strength and density were calculated by summing the weights, or number of nonzero values, of the edges between neurons and astrocytes, and was divided by $(N_n + N_a) = 2$, where N_n is the number of neurons and N_a is the number of astrocytes, to normalize for network size. More global network statistics, such as betweenness centrality, global efficiency, and clustering coefficient, cannot be separated into intra- and interlayer components. These metrics were calculated for the entire multilayer network and also for individual layers. To estimate the effect of treatment group assignment on these graph statistics (*B*, *C*, and *E*), we ran a generalized linear regression using MATLAB's *glmfit*. The link function was the identity and error distribution was assumed to be normal. Outcome variables *B*, *C*, and *E* were regressed against categorical variables indicating treatment group (MEM, No Injury (Sham); MPEP, No Injury (Sham); MEM, Injury; or MPEP, Injury), as well as network density or strength, to control for its effects on topological statistics. Regression coefficient estimates and *p*-values are reported above.

Community detection in spatial and functional graphs

To better understand how individual astrocyte segments and neurons give rise to collective network structure, we analyzed the multilayer network's mesoscale community structure. In addition to functional connectivity, we analyzed the spatial proximity of neurons and astrocyte segments in culture, based on the well-supported notion that spatial embedding influences network topology (*44*). In many cases, the community structure of networks is shaped by spatial embedding, with closely situated nodes tending to cluster functionally (*45*). To test whether astrocyte segments and neurons are functionally independent of their spatial communities, we compared the community structure of functionally and spatially derived neuron-astrocyte networks and found them to be different.

Furthermore, comparing spatial and functional network modularity in astrocyte segments facilitated more general characterization of astrocyte calcium signaling. Astrocytic calcium events are heterogeneous in temporal and spatial profile, ranging from fast, locally restricted events to slower, cell-wide waves, with these two types of events often occurring independently (*33, 39*). There is limited understanding of how Ca^{2+} fluctuations in microdomains relate to cell-wide, or population-wide, astrocyte calcium events. Analyzing astrocyte segments as nodes in a spatially embedded network enabled us to elucidate the extent to which segments of the same astrocyte are functionally interdependent.

Modules are communities of nodes that are functionally or spatially more interconnected to each other than to other nodes in the network. Modules were generated by maximizing the modularity quality function using both spatial and functional adjacency matrices for single-layer neuron and astrocyte networks, and for multilayer networks. The parameter γ

is a resolution parameter that governs the size and number of detected communities. For both single-layer and multilayer networks, γ was tuned separately and manually for spatially and functionally generated graphs to minimize the difference between the number of communities detected for spatial and functional networks. Quality was maximized by placing nodes into communities such that the quality Q is as large as possible, using an iterative Louvain-like community detection algorithm implemented in MATLAB (*25*). A Girvan-Newman (*24*) null model was used for both functional and spatial graphs and implemented in a custom MATLAB script (SM sec. I). Because the modularity landscape is rough (*47*), the heuristic can detect a different partition each time it is applied. Thus, here we assign a node's module to be the mode over 50 maximizations. Nevertheless, module assignment still varies slightly between batches of 50 trials, a property that more generally has been demonstrated for small networks (*47*). In addition to the value of Q, the Louvain algorithm outputs the partition g, a vector containing the community number of each node.

We compared the similarity of the partitions predicted by functional and structural graphs by calculating their Adjusted Rand Index (*ARI*) using MATLAB's *Randindex* function. The Rand Index represents the probability that the two partitions, functional and spatial, will agree on the community of a randomly chosen node. A Rand Index of zero indicates that the two partition vectors do not have any groupings in common, while a value of one indicates complete agreement. The *ARI* corrects for over-inflation due to chance assignment (SM sec. I). Module participation was calculated as the fraction of all modules that contain at least one of that cell type.

Statistical Testing

Two-sided one-sample t-tests were conducted to determine the statistical significance of the difference between actual and null network statistics, as well as the statistical significance of the difference of the mean ARI from zero for neuron layer (n = 36 dishes), astrocyte layer (n = 23 dishes) and multilayer (n = 27 dishes) networks. Two-sided paired t-tests were conducted to determine whether there existed a statistically significant difference between the size of functionally and spatially determined modules for neuron (n = 36 dishes), astrocyte (n = 23 dishes), and multilayer (n = 27 dishes) networks. A two-sided unpaired t-test was used to test for a statistically significant difference between the size of multilayer network functional communities in MPEP- and MEM-treated dishes. One-way analysis of variance (ANOVA) was used to test for a significant difference between means of a single measure between multiple groups. Two-way ANOVA was used to test for a significant difference between means of multiple measures between multiple groups. The Holm-Sidak method was used to correct for multiple comparisons when making post-ANOVA comparisons between the means of selected pairs of groups. The Tukey method was used to correct for multiple comparisons when making post-ANOVA comparisons between every mean and every other mean. Two-sided t-tests were used to test for statistical significance of all regression coefficients.

Supplementary Materials

Materials and Methods

Fig. S1. Example conversion of spike train to neuronal adjacency matrices for a single dish.

Fig. S2. $mGluR_5$ inhibition and injury decrease neuronal but not astrocytic activity level.

Table S1. Results of a generalized linear regression to predict the effect of group assignment on mean clustering coefficient (*C*), mean normalized betweenness centrality (*B*), and global efficiency (*E*) for neuronal networks.

Fig. S3. Community structure of *in vitro* neuronal networks.

Fig. S4. Astrocyte functional network topology.

Table S2. Results of generalized linear regression to predict the effect of group assignment on mean clustering coefficient (*C*), mean normalized betweenness centrality (*B*), and global efficiency (*E*) for astrocyte networks.

Table S3. Results of generalized linear regression to predict the effect of group assignment on mean clustering coefficient (*C*), mean normalized betweenness centrality (*B*), and global efficiency (*E*) for multilayer networks.

Table S4. Results of generalized linear regression to predict the effect of group assignment on mean clustering coefficient (*C*), mean normalized betweenness centrality (*B*), and global efficiency (*E*) for weighted neuron networks.

Fig. S5. Immunofluorescent staining confirms expression of $mGluR_5$ in neurons and astrocytes.

Fig. S6. *In vitro* calcium image acquisition and processing of neuron-astrocyte networks.

References and Notes

1. J. T. Porter, K. D. McCarthy, Hippocampal astrocytes *in situ* respond to glutamate released from synaptic terminals. *J. Neurosci.* **16**, 5073–5081 (1996).
2. J. Kang, L. Jiang, S. A. Goldman, M. Nedergaard, Astrocyte-mediated potentiation of inhibitory synaptic transmission. *Nat. Neurosci.* **1**, 683–692(1998).
3. G. Perea, A. Araque, Astrocytes potentiate transmitter release at single hippocampal synapses. *Science* **317**, 1083–1086 (2007).

50 4. M. A. Di Castro, J. Chuquet, N. Liaudet, K. Bhaukaurally, M. Santello, D. Bouvier, P. Tiret,
51 A. Volterra, Local Ca^{2+} detection and modulation of synaptic release by astrocytes. *Nat.*
52 *Neurosci.* **14**, 1276–1284 (2011).
53 5. A. Panatier, J. Vallée, M. Haber, K. K. Murai, J.-C. Lacaille, R. Robitaille, Astrocytes are
54 endogenous regulators of basal transmission at central synapses. *Cell* **146**, 785–798 (2011).
55 6. A. Panatier, R. Robitaille, Astrocytic $mGluR_5$ and the tripartite synapse. *Neuroscience* **323**,
56 29–34 (2016).
57 7. O. Pascual, K. B. Casper, C. Kubera, J. Zhang, R. Revilla-Sanchez, J.-Y. Sul, H. Takano, J.
58 Moss, K. McCarthy, P. G. Haydon, Astrocytic purinergic signaling coordinates synaptic
59 networks. *Science* **310**, 113–116 (2005).
70 8. A. Serrano, N. Haddjeri, J.-C. Lacaille, R. Robitaille, GABAergic network activation of glial
71 cells underlies hippocampal heterosynaptic depression. *J. Neurosci.* **26**, 5370–5382 (2006).
72 9. K. E. Poskanzer, R. Yuste, Astrocytic regulation of cortical up states. *PNAS* **108**, 18453–
73 18458 (2011).
74 10. R. Balázs, S. Miller, C. Romano, A. De Vries, Y. Chun, C. W. Cotman, Metabotropic
75 glutamate receptor $mGluR_5$ in astrocytes: Pharmacological properties and agonist regulation.
76 *J. Neurochem.* **69**, 151–163 (1997).
77 11. X. Wang, N. Lou, Q. Xu, G.-F. Tian, W. G. Peng, X. Han, J. Kang, T. Takano, M. Ned-
78 ergaard, Astrocytic Ca^{2+} signaling evoked by sensory stimulation *in vivo*. *Nat. Neurosci.* **9**,
79 816–823(2006).
80 12. J. E. Burda, A. M. Bernstein, M. V. Sofroniew, Astrocyte roles in traumatic brain injury.
81 *Exp. Neurol.* **275**, 305–315 (2016).
82 13. D. Myer, G. G. Gurkoff, S. Lee, D. Hovda, M. V. Sofroniew, Essential protective roles of
83 reactive astrocytes in traumatic brain injury. *Brain* **129**, 2761–2772 (2006).

14. T. P. Patel, S. C. Ventre, D. F. Meaney, Dynamic changes in neural circuit topology following mild mechanical injury *in vitro*. *Ann. Biom. Eng.* **40**, 23–36 (2012).

15. W. H. Kang, W. Cao, O. Graudejus, T. P. Patel, S. Wagner, D. F. Meaney, B. Morrison III, Alterations in hippocampal network activity after *in vitro* traumatic brain injury. *J. Neurotrauma* **32**, 1011–1019 (2015).

16. A. C. Charles, J. E. Merrill, E. R. Dirksen, M. J. Sandersont, Intercellular signaling in glial cells: Calcium waves and oscillations in response to mechanical stimulation and glutamate. *Neuron* **6**, 983–992 (1991).

17. E. Ellis, J. McKinney, K. Willoughby, S. Liang, J. Povlishock, A new model for rapid stretch-induced injury of cells in culture: Characterization of the model using astrocytes. *J. Neurotrauma* **12**, 325–339 (1995).

18. B. Rzigalinski, J. Weber, K. Willoughby, E. Ellis, Intracellular free calcium dynamics in stretch-injured astrocytes. *J. Neurochem.* **70**, 2377–2385 (1998).

19. D. S. Bassett, P. Zurn, J. I. Gold, On the nature and use of models in network neuroscience. *Nat. Rev. Neurosci.* **19**, 566–578 (2018).

20. M. Kivelä, A. Arenas, M. Barthelemy, J. P. Gleeson, Y. Moreno, M. A. Porter, Multilayer networks. *J. Complex Networks* **2**, 203–271 (2014).

21. M. Vaiana, S. F. Muldoon, Multilayer brain networks. *J. Nonlinear Sci.* **28,** 1–23 (2018).

22. R. F. Betzel, D. S. Bassett, Multi-scale brain networks. *Neuroimage* **160**, 73–83 (2017).

23. S. F. Muldoon, D. S. Bassett, Network and multilayer network approaches to understanding human brain dynamics. *Philos. Sci* **83**, 710–720 (2016).

24. M. E. Newman, M. Girvan, Finding and evaluating community structure in networks. *Phys. Rev. E* **69**, 026113 (2004).

25. I. S. Jutla, L. G. Jeub, P. J. Mucha, A generalized Louvain method for community detection implemented in MATLAB, http://netwiki.amath.unc.edu/GenLouvain (2011).

26. W. M. Rand, Objective criteria for the evaluation of clustering methods. *J. Am. Stat. Assoc.* **66**, 846–850 (1971).

27. E. Shigetomi, E. A. Bushong, M. D. Haustein, X. Tong, O. Jackson-Weaver, S. Kracun, J. Xu, M. V. Sofroniew, M. H. Ellisman, B. S. Khakh, Imaging calcium microdomains within entire astrocyte territories and endfeet with GCaMPs expressed using adeno-associated viruses. *J. Gen. Physiol.* **141**, 633–647 (2013).

28. A. M. Choo, W. J. Miller, Y.C. Chen, P. Nibley, T. P. Patel, C. Goletiani, B. Morrison III, M. K. Kutzing, B. L. Firestein, J.-Y. Sul, et al., Antagonism of purinergic signalling improves recovery from traumatic brain injury. *Brain* **136**, 65–80 (2013).

29. S. M. Rodrigues, E. P. Bauer, C. R. Farb, G. E. Schafe, J. E. LeDoux, The Group I metabotropic glutamate receptor $mGluR_5$ is required for fear memory formation and long-term potentiation in the lateral amygdala. *J. Neurosci.* **22**, 5219–5229 (2002).

30. Z. Jia, Y. Lu, J. Henderson, F. Taverna, C. Romano, W. Abramow-Newerly, J. M. Wojtowicz, J. Roder, Selective abolition of the NMDA component of long-term potentiation in mice lacking $mGluR_5$. *Learn. Mem.* **5**, 331–343 (1998).

31. V. A. Movsesyan, D. M. O'Leary, L. Fan, W. Bao, P. G. Mullins, S. M. Knoblach, I. Faden, $mGluR_5$ antagonists 2-methyl-6-(phenylethynyl)-pyridine and (e)-2-methyl-6-(2-phenylethenyl)-pyridine reduce traumatic neuronal injury *in vitro* and *in vivo* by antagonizing n-methyl-d-aspartate receptors. *J. Pharmacol. Exp. Ther.* **296**, 41–47 (2001).

32. P. M. Lea IV, S. J. Custer, S. Vicini, A. I. Faden, Neuronal and glial $mGluR_5$ modulation prevents stretch-induced enhancement of NMDA receptor current. *Pharmacol. Biochem. Behav.* **73**, 287–298 (2002).

33. N. Bazargani, D. Attwell, Astrocyte calcium signaling: the third wave. *Nat. Neurosci.* **19**, 182–189 (2016).

34. A. Araque, G. Carmignoto, P. G. Haydon, S. H. Oliet, R. Robitaille, A. Volterra, Gliotransmitters travel in time and space. *Neuron* **81**, 728–739 (2014).

35. R. D. Fields, D. H. Woo, P. J. Basser, Glial regulation of the neuronal connectome through local and long-distant communication. *Neuron* **86**, 374–386 (2015).

36. S. Mederos, A. Hernandéz-Vivanco, J. Ramírez-Franco, M. Martn-Fernandéz, M. Navarrete, A. Yang, E. S. Boyden, G. Perea, Melanopsin for precise optogenetic activation of astrocyte-neuron networks. *Glia* **67**, 915-934 (2019).

37. J. Schummers, H. Yu, M. Sur, Tuned responses of astrocytes and their influence on hemodynamic signals in the visual cortex. *Science* **320**, 1638–1643 (2008).

38. G. Perea, A. Yang, E. S. Boyden, M. Sur, Optogenetic astrocyte activation modulates response selectivity of visual cortex neurons *in vivo*. *Nat. Commun.* **5**, 3262 (2014).

39. B. S. Khakh, M. V. Sofroniew, Diversity of astrocyte functions and phenotypes in neural circuits. *Nat. Neurosci.* **18**, 942–952 (2015).

40. W. Sun, E. McConnell, J.-F. Pare, Q. Xu, M. Chen, W. Peng, D. Lovatt, X. Han, Y. Smith, M. Nedergaard, Glutamate-dependent neuroglial calcium signaling differs between young and adult brain. *Science* **339**, 197–200 (2013).

41. D. Kugiumtzis, A. Tsimpiris, Measures of Analysis of Time Series (MATS): a MATLAB toolkit for computation of multiple measures on time series data bases. arXiv preprint *arXiv:***1002.1940** (2010).

42. S. Maslov, K. Sneppen, Specificity and stability in topology of protein networks. *Science* **296**, 910–913 (2002).

43. M. Rubinov, O. Sporns, Complex network measures of brain connectivity: Uses and interpretations. *NeuroImage* **52**, 1059–1069 (2010).

44. M. Barthélemy, Spatial networks. *Phys. Rep.* **499**, 1–101 (2011).

45. P. Expert, T. S. Evans, V. D. Blondel, R. Lambiotte, Uncovering space-independent communities in spatial networks. *PNAS* **108**, 7663–7668 (2011).
46. B. H. Good, Y.-A. De Montjoye, A. Clauset, Performance of modularity maximization in practical contexts. *Phys. Rev. E* **81**, 046106 (2010).
47. J.P. Onnela, J. Saramäki, J. Kertész, K. Kaski, Intensity and coherence of motifs in weighted complex networks. *Phys. Rev. E* **71**, 065103 (2005).
48. D. Dzamba, P. Honsa, M. Anderova, NMDA receptors in glial cells: Pending questions. *Curr. Neuropharmacol.* **11**, 250–262 (2013).
49. C. Bowman, H. Kimelberg, Excitatory amino acids directly depolarize rat brain astrocytes in primary culture. *Nature* **311**, 656–659 (1984).
50. H. Kettenmann, M. Schachner, Pharmacological properties of gamma-aminobutyric acid-, glutamate-, and aspartate-induced depolarizations in cultured astrocytes. *J. Neurosci.* **5**, 3295–3301 (1985).
51. K. Backus, H. Kettenmann, M. Schachner, Pharmacological characterization of the glutamate receptor in cultured astrocytes. *J. Neurosci. Res.* **22**, 274–282 (1989).
52. V. D. Blondel, J.-L. Guillaume, R. Lambiotte, E. Lefebvre, Fast unfolding of communities in large networks. *J. Stat. Mech: Theory Exp.* **2008**, P10008 (2008).
53. S. Fortunato, Community detection in graphs. *Phys. Rep.* **486**, 75–174 (2010).

Acknowledgments

General: We thank S. Schumm, K. Wiley, and P. Srivastava for helpful comments on an earlier version of this manuscript; A. Nam for primary cell culture; and O. Teter for collaborative brainstorming.

Funding: This work was supported by a Paul G. Allen Family Foundation grant to DFM and DSB. DFM would like to acknowledge the support of the NINDS (1RO1-NS 088276). DSB would also like to acknowledge support from the John D. and Catherine T. MacArthur Foundation, the Alfred P. Sloan Foundation, the ISM Foundation, the Army Research Laboratory (W911NF-10-2-0022), the Army Research Office (Bassett-W911NF-14-1-0679, Grafton-W911NF-16-1-0474, DCIST- W911NF-17-2-0181), the Office of Naval Research, the National Institute of Mental Health (2-R01-DC-009209-11, R01-MH112847, R01-MH107235, R21-M MH-106799), the National Institute of Child Health and Human Development (1R01HD086888-01), National Institute of Neurological Disorders and Stroke (R01 NS099348), and the National Science Foundation (BCS-1441502, BCS-1430087, NSF PHY-1554488 and BCS-1631550)). The content is solely the responsibility of the authors and does not necessarily represent the official views of any of the funding agencies.

Author contributions: MES and DFM conceived the experiment(s), MES conducted the experiment(s), DSB and MES conceived the network analysis, MES analyzed the results and wrote the manuscript. All authors interpreted results and revised the manuscript.

Data and materials availability: Data available upon reasonable request. Please contact the corresponding author.

Figures

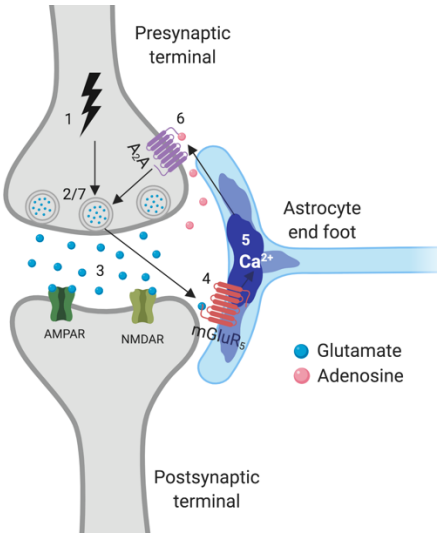

Fig. 1. The Tripartite Synapse mediated through mGluR$_5$. An action potential arrives at the presynaptic terminal (1) and triggers glutamate release (2-3). Glutamate acts on astrocytic mGluR$_5$ (4), leading to an increase in astrocyte Ca^{2+} (5). The astrocyte releases adenosine (6), which is taken up by presynaptic A_2A receptors, and alters the probability of neurotransmitter release (7). Created with BioRender.

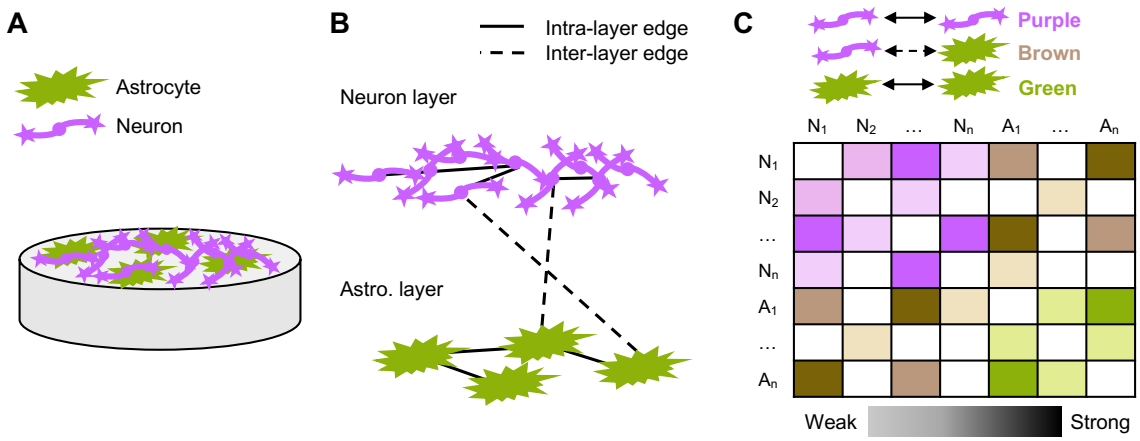

Fig. 2. A multilayer network model of neurons and astrocytes in co-culture. (**A**) Simplified schematic of neurons (purple) and astrocytes (green) in co-culture. Morphology and size are exaggerated. (**B**) Cells are separated into two distinct layers based on their identity. Layers are made up of exclusively one cell type. Each cell may be connected to cells in its own layer or to cells in the other layer. Intralayer edges are depicted with full lines and interlayer edges with dashed lines. (**C**) Example adjacency matrix for the multilayer network shown in panel **(B)**. The green and red weights correspond to intralayer edges and the yellow weights correspond to interlayer edges. Color saturation indications strength of connection.

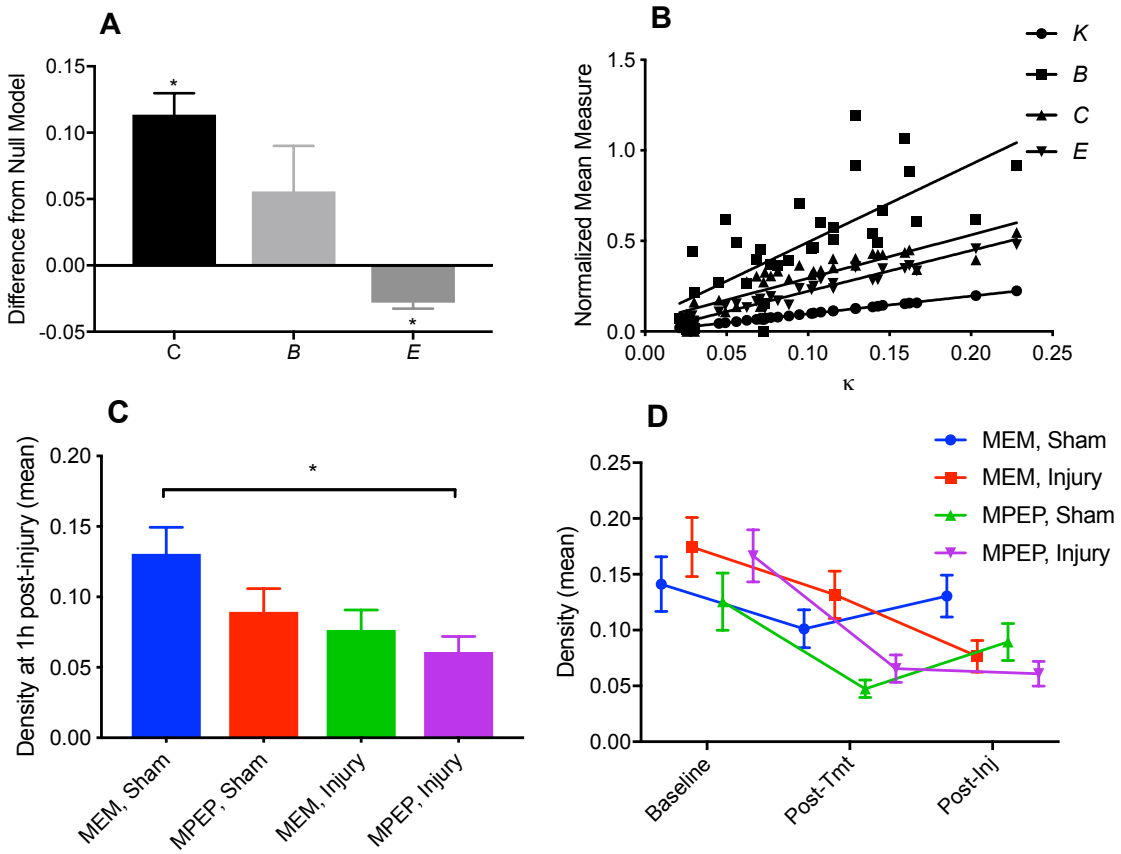

Fig. 3. Effect of mGluR$_5$ inhibition and injury on neuron network topology. (**A**) Difference from random null model of calculated mean clustering coefficient *C*, normalized betweenness centrality *B*, and global efficiency *E*. We observe significantly larger clustering coefficients (one-sample t-test on differences between actual values and null model values of *C*: $t = 7.10$, $df = 35$, $p < 0.0001$) and significantly lower global efficiency (one-sample t-test on differences between actual values and null model values of *E*: $t = 6.16$, $df = 35$, $p < 0.0001$) than expected in the null model. (**B**) Mean clustering coefficient *C*, normalized betweenness centrality *B*, normalized degree *K*, and global efficiency *E* vs. mean density for each dish at the third time point. We observe clear positive correlations as assessed by a linear regression for degree *K* ($R^2 = 0.999$, $F(1,32) = 40933$, $p < 0.0001$), betweenness centrality *B* ($R^2 = 0.5703$, $F(1,32) = 42.47$, $p < 0.0001$), clustering coefficient *C* ($R^2 = 0.7914$, $F(1,32) = 121.4$, $p < 0.0001$) and global efficiency *E* ($R^2 = 0.9308$, $F(1,32) = 430.3$, $p < 0.0001$). (**C**) Mean density of each dish is significantly

lower in injured dishes treated with MPEP compared to control conditions (Tukey's multiple comparisons test, $q = 4.70$, $df = 32$, $p = 0.0114$). (**D**) Mean density of each group at baseline, following treatment with MEM or MPEP, and one hour following injury or sham. There was a significant effect of time (two-way ANOVA, $F(2, 96) = 14.9$, $p < 0.0001$), group assignment (two-way ANOVA, $F(3, 96) = 3.097$, $p = 0.0305$), and the interaction between the two (two-way ANOVA, $F(6,96) = 2.251$, $p = 0.0447$) on density. At the second time point, there was a significant difference between MPEP/Sham and MEM/Injury groups (Tukey's multiple comparisons test, $q = 4.276$, $df = 96$, $p = 0.0166$). Error bars indicate standard error of the mean (SEM) and asterisks indicate statistical significance. Tmt: treatment; MEM: treated with minimum essential media; MPEP: treated with anti-mGluR$_5$; Injury: subjected to targeted neuronal tap injury; Sham: negative injury control.

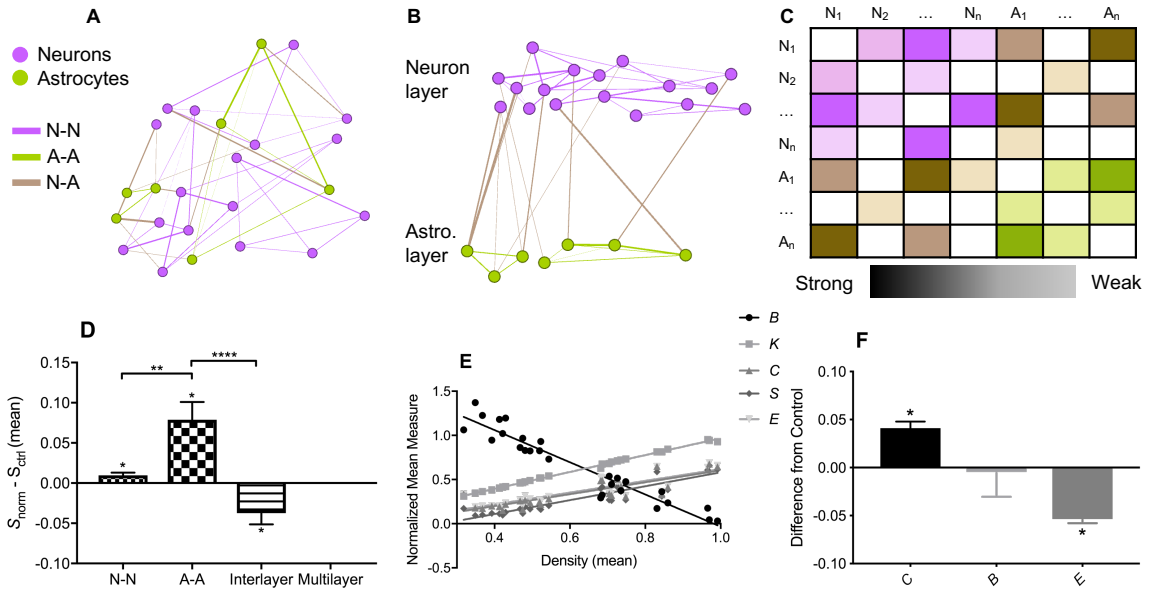

Fig. 4. Topology of multilayer neuron-astrocyte networks. (**A**) Representative graph of a multilayer network with weighted connections. (**B**) The multilayer graph shown in panel a, separated into neuronal and astrocytic layers. (**C**) Flattened adjacency matrix for the multilayer network shown in panels (**A**) and (**B**). Interlayer connections are colored brown. (**D**) Difference in mean normalized strength of neuron layer (blue), astrocyte layer (red), interlayer (purple), and multilayer (purple) connections, from a randomized network with preserved degree distribution and density. Nodal strength in the neuron network (one-sample t-test on differences between actual values and null values of *S*, $t = 2.995$, $df = 26$, $p = 0.0060$) and in the astrocyte network (one-sample t-test on differences between actual and null *S*, $t = 3.569$, $df = 26$, $p = 0.0014$) layers was higher than randomized controls. In contrast, the mean nodal strength between layers was lower than randomized controls (one-sample t-test on differences between actual values and null model values of *S*, $t = 2.716$, $df = 26$, $p = 0.0116$). Nodal strength in the astrocyte layer was significantly higher than that in the neuronal layer (Holm-Sidak multiple comparisons test, $q = 5.264$, $df = 104$, $p = 0.0018$), and than that in interlayer connections (Holm-Sidak multiple comparisons test, $q = 8.863$, $df = 104$, $p < 0.0001$). (**E**) Correlation of multilayer network statistics with density. Mean clustering coefficient (*C*), normalized betweenness centrality (*B*), normalized strength (*S*),

and global efficiency (E) versus mean density for each dish at the third time point. We observed clear positive correlations between density and graph statistics (results of linear regression for S, $R^2 = 0.8405$, $F(1,25) = 131.7$; for K, $R^2 = 0.9967$, $F(1,25) = 7552$; for B, $R^2 = 0.9108$, $F(1,25) = 255.2$; for C, $R^2 = 0.7290$, $F(1,25) = 67.24$; for E, $R^2 = 0.7442$, $F(1,25) = 72.74$; note that $p < 0.0001$ for all). (**F**) Difference in C, B, and E between multilayer networks and randomized controls. Multilayer networks exhibit significantly larger clustering coefficient C (one-sample t-test on differences between actual values and null model values, $t = 6.033$, $df = 26$, $p < 0.0001$) and significantly lower global efficiency E (one-sample t-test on differences between actual values and null model values, $t = 12.19$, $df = 26$, $p < 0.0001$) than their randomized counterparts, but did not differ in betweenness centrality B. Error bars indicate standard error of the mean (SEM) and asterisks indicate statistical significance.

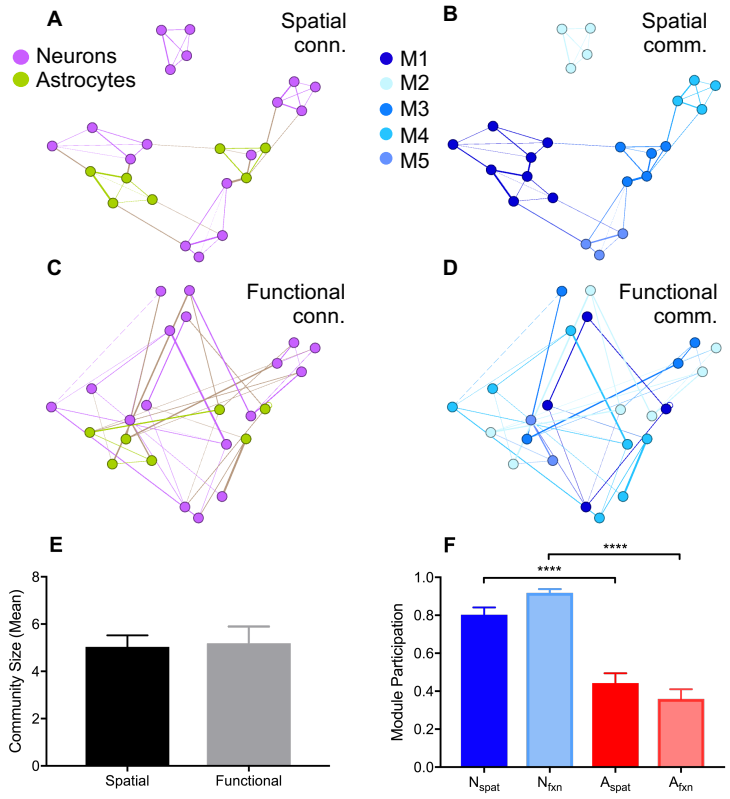

Fig. 5. Multilayer community structure and composition. (**A**) A representative graph of a multilayer network with weighted edges based on spatial proximity. (**B**) Community structure of the network shown in panel (**A**), with modules determined based on spatial proximity. Nodes of the same color belong to the same spatial module. (**C**) A representative graph of a multilayer network with weighted edges based on functional connectivity. (**D**), Community structure of the network shown in panel (**C**), with modules determined based on functional connectivity. Nodes of the same color belong to the same functional module. If functional connectivity were based on spatial proximity, the modules in panels (**B**) and (**D**) would be the same or highly similar. (**E**) Mean community size does not differ significantly between functional and spatial multilayer communities, as the spatial tuning parameter was adjusted to minimize this difference (paired t-test, $t = 0.1645$, $df = 22$, $p = 0.8709$). (**F**) Average module participation, the fraction of modules that contain at least one of that cell type, as determined based on spatial distance and functional connectivity for both neurons and astrocytes. Neurons

have significantly higher participation in both spatial and functional communities (Tukey's multiple comparisons test for the functional communities, $q = 8.549$, and for the spatial communities, $q = 11.28$; note that in both cases, $df = 88$, $p < 0.0001$), reflective of their abundance relative to astrocytes. Error bars indicate standard error of the mean (SEM) and asterisks indicate statistical significance.

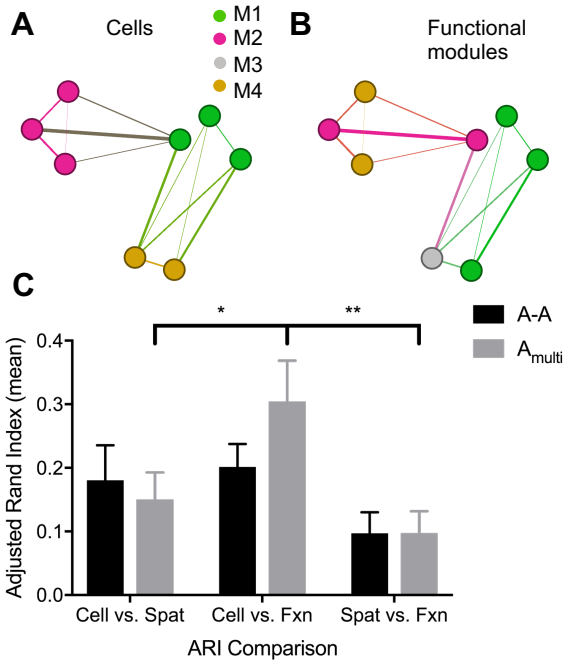

Fig. 6. Independence of functional and spatial communities of same-cell astrocyte segments. (**A**) A representative astrocyte network with the indicated community structure based on morphology of segments. Nodes (astrocyte segments) of the same color belong to the same cell. (**B**) The network in panel a with modules detected based on functional connectivity. Nodes (astrocyte segments) of the same color belong to the same functional module, independent of cell membership. (**C**), Mean Adjusted Rand Index (*ARI*) for morphologically connected astrocyte segment communities (cell) versus spatially-connected communities, morphologically-connected versus functionally-connected segment communities, and functionally-connected versus spatially-connected communities. Morphological versus spatial *ARI* is larger than morphological versus functional, and also than functional versus spatial *ARI*s in both independent astrocyte (black) and multilayer (gray) astrocyte modules (two-way ANOVA comparing the effect of module type and single- or multilayer network on *ARI*: $F(1,132) = 7.675$, $p = 0.0062$). The *AR*I is always larger for astrocyte communities generated using a multilayer network, though the improvement in *ARI* is not statistically significant (two-way ANOVA comparing the effect of single versus multilayer network type on ARI: $F(2,132) = 2.911$, p

23 = 0.0579). Error bars indicate standard error of the mean (SEM) and asterisks indicate

24 statistical significance.

25

26

Supplementary Materials

Materials and Methods

A. Network Statistics. Mean degree is the mean number of edges emerging from each node, or number of other nodes to which each node is connected. It is defined mathematically as:

$$\langle K \rangle = \frac{1}{n}\sum_{i=1}^{N} A_{ij}\,, [\mathbf{1}]$$

where A_{ij} is the binary weight between nodes i and j, and where n is the total number of nodes in the network. A high value of $\langle K \rangle$, which we normalize to N, means that on average, nodes in the network are connected to a large proportion of other nodes in the network.

Density is the ratio of the number of actual edges in the network to the total number of potential edges in the network. The number of potential edges in the network is proportional to the number of nodes: each node can be connected to each of the other nodes, but not itself. It is defined mathematically as:

$$\kappa = \frac{R}{N(N-1)}, [\mathbf{2}]$$

where R is the total number of edges in the network. Conceptually, density is an indicator of how strongly connected the network is. A network with high density has strongly interconnected nodes, while a network with low density has less strongly interconnected

nodes. Note that the calculation of density is the same for weighted and binary networks, as all weighted connections are counted equivalently.

Nodal strength is similar to degree, but accounts for connection weight in weighted graphs. Nodal strength is the sum of the weights of all of a node's edges in a weighted network. Conceptually, strength can be thought of as a weighted degree. It is defined mathematically as:

$$S(i) = \frac{1}{N-1}\sum_{j=1}^{N} A_{ij} \,.\, [\mathbf{3}]$$

In this work, we calculated the average network strength over all nodes, normalized by network size N. It is important to normalize by N because larger networks have a greater number of weighted connections and therefore a higher upper bound for $\langle S \rangle$. A network with high normalized $\langle S \rangle$ has many nodes with either many connections (high degree), a number of strong connections (large weight values), or both, for its size. Conversely, a network with low normalized $\langle S \rangle$ has many nodes with either few connections (low degree), a number of weak connections (low weight values), or both, for its size.

Mean clustering coefficient is the mean ratio of the number of actual triangles around each node to the total number of potential triangles around each node. It measures how many sets of three nodes are fully interconnected, or where each of the three nodes is connected

to the other two, and thus can be conceptualized as a local density measure. It is defined mathematically as:

$$C = \frac{1}{n}\sum_{i=1}^{N}\frac{2u_i}{k_i(k_i-1)}, [\mathbf{4}]$$

where k_i is the degree of node *i* and u_i is the number of triangles containing node *i*. The clustering coefficient is generalized to weighted networks by replacing the number of triangles u_i with the sum of triangle intensities (*47*). The average weighted clustering coefficient is calculated as:

$$C = \frac{1}{n}\sum_{i=1}^{N}\frac{2}{k_i(k_i-1)}\sum_{j,k}\left(\widetilde{w}_{ij}\widetilde{w}_{jk}\widetilde{w}_{ki}\right)^{1/3}, [\mathbf{5}]$$

where the weights are scaled by the largest weight in the network, $\widetilde{w}_{ij} = \widetilde{w}_{ij}/max(\widetilde{w}_{ij})$. Conceptually, by this definition, a node's weighted clustering coefficient is the unweighted version renormalized by the average intensity of triangles at that node. Here, we calculated the mean clustering coefficient, $\langle C \rangle$, in each of our networks. A network with a high value of $\langle C \rangle$ has a large proportion of fully connected triangles, or high local density, while a network with a low value of $\langle C \rangle$ has a small proportion of fully connected triangles, or low local density.

Betweenness centrality is a measure of how many shortest path lengths pass through a given node. Conceptually, betweenness centrality measures the degree to which a node

acts as a hub, facilitating many shortest-path connections between other nodes. It is defined as:

$$b_i = \frac{1}{(n-1)(n-2)} \sum_{h \neq j, h \neq i, j \neq i}^{N} \frac{l_{hj}(i)}{l_{hj}}, [\mathbf{6}]$$

where l_{hj} is the number of shortest paths between nodes h and j, and $l_{hj}(i)$ is the number of shortest paths between node h and node j that pass through node i. The shortest path length between nodes i and j is the minimum number of nodes that must be passed through to connect nodes i and j. For weighted networks, betweenness centrality was calculated as above, using the weighted distance matrix, computed using the BCT's distance_wei function, which uses Dijkstra's shortest path algorithm. Brandes's algorithm was used to compute centrality from the weighted distance matrix via the BCT's *betweenness_wei* function. We calculated the mean nodal betweenness centrality, $\langle B \rangle$, for each of our networks. We normalized by the number of nodes in the network N because a larger network has a greater number of shortest paths and therefore a larger upper bound on $\langle B \rangle$. A network with a high value of normalized $\langle B \rangle$ has a large proportion of nodes that act as hubs, with several shortest paths passing through them, while a network with a small value of $\langle B \rangle$ has a low proportion of hub-like nodes.

Global efficiency is the inverse of the harmonic mean of the shortest path length between any two nodes. The name refers to the fact that a network with a high characteristic shortest path length will, under some specific assumptions of dynamics, be slower to transmit information from node i to node j than a network with many short paths between nodes. Networks with few long-distance connections typically have many large shortest

path lengths. Reaching node j from node i in such a network requires many steps through other nodes, lessening its supposed efficiency. Global efficiency is defined as:

$$E = \frac{1}{n}\sum_{i=1}^{n}\frac{\sum_{i\neq j}^{N} d_{ij}^{-1}}{n-1}, [\mathbf{7}]$$

where d_{ij} is the shortest topological distance between nodes nodes i and j. Global efficiency of weighted networks is calculated as above with di j being a weighted path length, calculated using Dijkstra's algorithm in the BCT's *efficiency_wei*. As described above, a network with a high value of E has many long topological connections, a short characteristic pathlength, and is faster, under some specific assumptions of the dynamics, to transmit information between any two nodes. Conversely, a network with a low value of E has few long topological connections, a large characteristic pathlength, and is slower, under some specific assumptions of the dynamics, to transmit information between any two nodes.

B. Calculation of binary functional connectivity for neuronal adjacency matrices.

The instantaneous phase is given by:

$$\phi_i(t,v) = 2\pi\frac{(t-t^w)}{(t^{w+1}-t^w)}, [\mathbf{8}]$$

where $\boldsymbol{v}$ indexes inter-spike interval and $\boldsymbol{t^w}$is the time of the wth spike. To compare the synchronization of two spike trains $\boldsymbol{x(t)}$ and $\boldsymbol{y(t)}$, their absolute phase difference is calculated as:

$$\psi_{x,y}(t) = mod\big(\left|\psi_x(t)-\psi_y(t)\right|, 2\pi\big), [\mathbf{9}]$$

where $\psi_{x,y}(t)$is constant if $x(t)$ and $y(t)$ are completely synchronized and will take on all values [0,2π] if $x(t)$ and $y(t)$ are completely independent. The pairwise synchronization

index between $x(t)$ and $y(t)$ is calculated as the circular variance of the absolute phase differences:

$$\gamma_{x,y} = \sqrt{\langle \cos \psi_{x,y}(t) \rangle^2 + \langle \sin \psi_{x,y}(t) \rangle^2}. \, [\mathbf{10}]$$

Geometrically, $\gamma_{x,y}$ is a vector from the origin to the average of the instantaneous phase differences when plotted on a unit circle. Furthermore, $\gamma_{x,y}$, which ranges from zero for completely independent time series to one for completely synchronized time series, was used as the weight of the edge between the two nodes $\boldsymbol{x}$ and $\boldsymbol{y}$ in the adjacency matrices.

C. Calculation of pairwise correlation for astrocyte and multilayer adjacency matrices. First, the background fluorescence, estimated from the mean fluorescence of 50 non-ROI regions in the field of view, was subtracted from each ROI's fluorescence. The change in fluorescence was scaled to background, and scaled change in fluorescence was filtered using an order five, 0.5Hz lowpass Butterworth filter, implemented in MATLAB. For a pair of ROIs $\boldsymbol{x}$ and $\boldsymbol{y}$ with time series $\boldsymbol{x(t)}$ and $\boldsymbol{y(t)}$, the Pearson's correlation coefficient (eq. 11) was calculated over a set of time lags from -1s to 1s:

$$\rho_{xy} = \frac{N \sum x(t)y(t) - (\sum x(t) \sum y(t))}{\sqrt{\{[N \sum x(t)^2 - (\sum x(t))^2][N \sum y(t)^2 - (\sum y(t))^2\}}}, \, [\mathbf{11}]$$

where N is the total number of time points and each sum is taken over N.

The maximum value of ρ_{xy} over all time lags was taken and compared to ρ_{xy} between $x(t)$ and 100 surrogate traces $y(t)$, generated using the same AAFT algorithm described above, at the same lag as the actual traces. We then calculated the *Z*-statistic for the maximum actual ρ_{xy} based on the distribution of ρ_{xy}'s generated using the surrogates and converted it to a p-value based on the standard normal distribution. The *p*-value is the probability that the observed ρ_{xy} came from a distribution of ρ_{xy}'s between $x(t)$ and a

randomly permuted $y(t)$ with the same frequency and amplitude spectra. If p was less than 0.001, A_{xy}, the weight of the edge between astrocyte segments x and y, was set equal to the maximum value of ρ_{xy}, and zero otherwise.

D. Contribution of using weighted vs. binary neuronal layer graphs to multilayer network results. To control for the effect of using weighted neural graphs in multilayer network analysis but not single-layer neuron analysis, we repeated the above procedure using weighted networks for the neurons, generated using the same procedure as for astrocyte and multilayer adjacency matrices. This step was necessary to show that the addition of the astrocyte layer, rather than the weighting of neuron graphs, improved prediction of *B* and *C* following experimental manipulation. We fit a generalized linear model to the graph statistics (*B*, *C*, and *E*) estimated from weighted neuron networks constructed from each dish at the third time point, with group assignment and mean nodal strength as regressors. Relative to binary neuron networks, the fit was improved, but not to the extent of multilayer networks (table S4). After controlling for strength, group assignment was a statistically significant predictor of B at the third time point (t-test on coefficients of a generalized linear model, effect of MPEP: $\beta = 0.209$, $t = 3.50$, $df = 22$, $p = 0.002$; Injury: $\beta = 0.158$, $t = 2.75$, $df = 22$, $p = 0.012$; MPEP + Injury: $\beta = -0.286$, $t = -3.56$, $df = 22$, $p = 0.002$). Similar to multilayer networks, the effect of MPEP reversed the effect of injury, as indicated by the change in sign of the interaction term's coefficient. As for binary neural networks and astrocyte networks, treatment condition was not a statistically significant predictor of *C* or *E*. Thus, for all measures but *B*, inclusion of the astrocyte layer and interlayer connections improved the fit relative to a generalized linear model of either layer alone. Taken together, these results suggest that multilayer changes

in *B* are mostly mediated by changes in the neuron layer, while changes in *C* and *E* are mediated by changes in both layers and the connections between them.

E. Contribution of relative abundance of neurons to multilayer network topology and community structure. To determine the impact on micro- and macroscale multilayer topology of there being many more active neurons than astrocyte segments, we sub-sampled the neuronal population so that neuron and astrocyte layers were of equal size. For a multilayer network with $\boldsymbol{n_a}$ active astrocyte segments, we randomly selected $\boldsymbol{n_a}$ neurons from the neuronal population and formed new adjacency matrices based on the connectivity of the sub-population of neurons and the original population of astrocyte segments. Mean nodal strength, degree, density, betweenness centrality, clustering coefficient, and global efficiency were re-calculated for the half-neuron, half-astrocyte networks. Likewise, we re-ran community detection analysis and re-calculated the *ARI* and cell type module participation for balanced networks. Neuron layers were sub-sampled 30 times and the average measures over 30 iterations are reported. While this analysis is not biologically realistic, it is a useful statistical exercise to determine the impact of the relative abundance of active neurons in our cultures.

As was found for actual multilayer networks, randomly sub-sampled multilayer networks with an equal number of neurons and astrocytes exhibited significantly larger clustering coefficient (one-sample t-test on differences between actual values and null values of *C*, $t = 4.242$, $df = 22$, $p = 0.0003$) and lower global efficiency (one-sample t-test on differences between actual values and null values of *E*, $t = 5.028$, $df = 22$, $p < 0.0001$) than their randomized counterparts, but were no different in the betweenness centrality *B*. Nodal strength in astrocyte layers (one-sample t-test on differences between actual values and

null values of S, $t = 4.092$, $df = 22$, $p = 0.0005$) was higher than randomized controls, while mean nodal strength between layers was lower than randomized controls (one-sample t-test on differences between actual values and null values of S, $t = 3.232$, $df = 22$, $p = 0.0038$). Nodal strength in the astrocyte layer was significantly higher than the strength of interlayer connections (Tukey's multiple comparisons test, $q = 8.087$, $df = 88$, $p < 0.0001$). As with full-sized multilayer networks, intralayer connections were stronger than interlayer connections, although astrocyte segments were no longer significantly more strongly interconnected than neurons. This finding suggests that the relative strength of intralayer connections compared to interlayer connections is not primarily driven by the greater abundance of neurons.

Interestingly, the graph statistics C, B, and E were less correlated with density in sub-sampled multilayer networks than their full-sized counterparts, as evidenced by lower R^2 values and higher p-values for linear coefficients of these measures regressed on mean network density. This finding may be due to the fact that these measures are more correlated with density in the neuron layer than they are in the astrocyte layer. As was done for full-sized multilayer networks, we analyzed the impact of experimental manipulations on sub-sampled multilayer network topology using a generalized linear regression, with mean nodal strength as a regressor. In sub-sampled multilayer networks, injury and the interaction of MPEP and injury were significant predictors of betweenness centrality after controlling for changes in mean nodal strength (generalized linear model, effect of injury: $\beta = 0.541$, $t = 2.12$, $df = 22$, $= 0.046$; MPEP + injury: $\beta = -0.863$, $t = -2.44$, $df = 22$, $p = 0.023$). This finding suggests that injury- and interaction-mediated changes in betweenness centrality are not primarily driven by the relative abundance of neurons in

our cultures, while changes in the clustering coefficient and MPEP-mediated changes in the betweenness centrality may be.

To assess the impact of the relative abundance of neurons in our cultures on community structure, we performed the same modularity detection on sub-sampled multilayer networks ($\gamma_s = 1.13, \gamma_f = 1.55$). The mean *ARI* between spatial and functional sub-sampled multilayer communities was significantly larger than for actual multilayer networks (mean for full multilayer = 0.05364, mean for sub-sampled multilayer = 0.1065, paired two-tailed t-test, $t = 2.346$, $df = 22$, $p = 0.0284$). This disagreement between spatial and functional partitioning was not driven by differences in community size, as γ, the spatial tuning parameter, was adjusted to reduce this difference (paired t-test, $t = 0.8896$, $df = 22$, $p = 0.3833$). The difference between actual and sub-sampled multilayer ARI may be due to differences in overall network size, or higher disagreement between spatial and functional modularity in neuronal layers. In sub-sampled multilayer networks, neurons and astrocyte segments participated equally in spatial and functional modules. Thus, differences in module participation in full multilayer networks reflects the dominance of neurons in quantity.

F. Immunocytochemistry. Cells were fixed in 4% paraformaldehyde (PFA) immediately following imaging and maintained in 1X phosphate-buffered saline (PBS) until staining. Cell membranes were permeabilized with cold 0.2% Triton X-100 in PBS for 5 min. Non-specific binding was blocked with 1% bovine serum albumin (BSA, Sigma Aldrich) and 2.5% normal goat serum (NGS) for 45 min at room temperature (RT). Primary antibodies were incubated at in diluted blocking solution (0.2% BSA and 0.5% NGS in PBS) overnight at 4°C at the following concentrations: Mouse-anti-MAP2 (Millipore Sigma) at

1:750, Rabbit-anti-GFAP (Abcam) at 1:500. Following a wash with diluted blocking solution, secondary antibodies were incubated in diluted blocking solution for 45 min at RT at the following concentrations: Goat-anti-mouse Alexa Fluor 568 (Thermo Fisher Scientific) at 1:1000 and Goat-anti-rabbit Alexa Fluor 633 (Thermo Fisher Scientific) at 1:1000. After a second wash, anti-mGluR$_5$ Alexa Fluor 488 (Novus Biologicals) was incubated at a concentration of 1:100. All antibody solutions were centrifuged at 15,000 rotations per minute for 10 min to remove aggregates. Following three rinses with PBS, stained cells were maintained under low light conditions until imaging. To stain for nuclei, 10 ug/mL Hoescht was applied during the final rinse step.

G. Automated detection of neuron and astrocyte calcium events. The spatial and temporal heterogeneity of astrocyte calcium signals impedes their identification and quantification. Nevertheless, to fully understand neuron-astrocyte signaling, astrocyte Ca^{2+} must be directly observed. We aimed to develop a robust quantitative algorithm for differentiating neuron and astrocyte calcium signals and counting astrocyte calcium events. As with neurons, while some information is lost when a calcium trace is converted to an event train, binarization reduces the complexity of the data and the subsequent computational load. Furthermore, event binarization enables calculation of metrics such as event rate, synchronization, and functional connectivity.

There are several existing methods for the automatic identification of neural spikes from various acquisition modalities. Our group recently developed FluoroSNNAP, Fluorescence Single Neuron and Network Analysis Package, an open-source, interactive software developed in MATLAB for automatic quantification of single-cell and population-level calcium dynamics (*14*). FluoroSNNAP showed improved calcium

transient detection with a template-based algorithm compared to peak-based or wavelet-based detection methods. Subsequently, we chose to develop an analogous template-based algorithm for automated detection of astrocyte calcium transients. This automated event detection algorithm is integrated into a semi-automated pipeline for analyzing large amounts of calcium image data from mixed cell populations.

To generate the astrocyte analog of this neuronal spike detection algorithm, a library of representative astrocyte calcium event templates was curated from actual calcium activity of IF-confirmed astrocytes. This library was used as templates in a previously developed template-matching algorithm for neuronal event detection (*14*). To validate our event detection algorithm, we assessed its performance on 10 recordings from five different isolations, each with one dish and two conditions. We recorded the number of correctly identified events, falsely identified events, and true events. The sensitivity and specificity of event detection were calculated for each trace (eqs. 12 & 13).

$$Sensitivity = \frac{TP}{TP + FN}, \mathbf{[12]}$$

and

$$Specificity = \frac{TN}{TN + FP}, \mathbf{[13]}$$

where TP is the number of true events correctly identified, FN is the number of true events missed, TN is the number of windows that were correctly identified as not having an event, and FP is the number of windows incorrectly identified as having an event.

To test the performance of the astrocyte event detection algorithm on fluorescence traces that were not used to generate the library, we assessed its performance on 10 recordings from five different isolations, each with one dish and two conditions. The signal-to-noise

ratio for all astrocyte ROIs in four of these recordings fell below the threshold for event detection. A total of 78 astrocyte traces in the remaining six recordings from four dishes were manually inspected. We recorded the number of correctly identified events, falsely identified events, and true events for each trace. We used recording identification as a pooling variable when averaging sensitivity and specificity to avoid bias towards recordings with more traces (more active astrocyte segments). Mean sensitivity of all recordings was 92.61% (95% CI: [0.90, 1.03]) and mean specificity was 96.35% (95% CI: [0.85, 1.00]).

H. A functional assay to differentiate neurons and astrocytes. Neurons and astrocytes respond differently to the application of N-Methyl-D-aspartic acid or N-Methyl-D-aspartate (NMDA). NMDA, an amino acid derivative, is a specific NMDA receptor (NMDAR) agonist that mimics the action of glutamate, the endogenous NMDAR ligand. Unlike glutamate, NMDA is specific to NMDARs and does not activate other glutamate receptors that may be present on neurons and astrocytes. Evidence of functional NMDAR expression in cultured cortical astrocytes is insufficient to confirm existence (*48*). Regardless of expression level, as observed here and in prior studies, NMDA does not directly excite astrocytes (*49-51*), but has an excitotoxic effect on neurons, greatly increasing their activity. With this knowledge, we can classify cells that exhibit increased calcium event frequency after NMDA application as neurons, and those that are inactive or maintain their basal activity level as astrocytes. Below we describe an experiment we

conducted to validate the use of NMDA as a functional terminal assay to distinguish between neurons and astrocytes in our cell culture model.

Primary cultures (n = 5) prepared as described in the Materials and Methods section were transduced with GCaMP6f on the CAG promoter at DIV 3 and imaged at 488nm, 50s exposure on DIV 7. Three minutes of baseline activity was recorded after a two-minute adjustment period on the stage. Cells were imaged immediately following addition of 100uM NMDA + 1uM glycine coagonist for up to five minutes. Calcium activity was extracted as described in the Materials and Methods (fig. S6). Maximum fluorescence projections generated in ImageJ software (National Institutes of Health) were manually identified, with neuronal cell bodies and astrocyte microdomains segmented as separate regions of interest (ROIs). Astrocyte segments were labeled using a custom MATLAB graphical user interface (GUI). The calcium activity of predicted astrocytes after NMDA application was examined and compared to that of a neuron. Predicted astrocyte ROIs that responded as a neuron would to NMDA application were reassigned as neurons.

Cells were fixed in 4% PFA and stained per the protocol described below for microtubule-associated protein 2 (MAP2, neurons; 1:1000 dilution for mouse-anti-MAP2 primary and donkey-anti-mouse secondary antibody) and GFAP (astrocytes; 1:500 dilution for rabbit-anti-GFAP primary antibody and 1:1000 dilution for goat-anti-rabbit secondary antibody). DNA was stained with Hoechst at 10ug/mL. Immunoflourescent (IF) images were obtained at 405 (DNA), 561 (neurons), and 640 (astrocytes) nm. To verify that ROIs

43 morphologically and functionally identified as astrocytes expressed GFAP, the same field
44 of view as imaged under GCaMP6f was relocated during IF imaging.
45
46 Following the application of NMDA, neuronal event rate increased significantly by a
47 mean of 16.89 events per minute (Sidak's multiple comparisons test; $t = 4.932$, $df = 8$, $p =$
48 0.0003). The effect of NMDA was easily identified by visual examination of single-cell
49 and population activity. Importantly, the calcium activity of astrocytes was unaltered from
50 baseline following addition of NMDA (mean difference = -1.493, Sidak's multiple
51 comparisons test; $t = 0.5897$, $df = 8$, $p = 0.8165$). After sorting cells based on NMDA
52 response, 100% of predicted astrocyte segments ($n = 79$) and 96% of neurons ($n = 604$)
53 were confirmed by IF staining ($n = 5$ dishes).
54
55 **I. Community detection methodology.** The modularity quality function is given by:
56 $$Q = \sum_{ij} [A_{ij} - \gamma P_{ij}] \delta(c_i, c_j), [\mathbf{14}]$$
57 where Q measures quality, A_{ij} is the observed adjacency matrix, P_{ij} is the null model
58 adjacency matrix, and $\delta(c_i, c_j)$ is one when nodes i and j are in the same community and
59 zero otherwise. The parameter γ is a resolution parameter that governs the size and
60 number of detected communities. The values of γ were 1.125 for spatial astrocyte graphs,
61 1.270 for functional astrocyte graphs, 1.170 for spatial neuron graphs, and 1.250 for
62 functional neuronal graphs. A Newman-Girvan (*32*) null model was used for both

functional and spatial graphs and it was implemented in a custom MATLAB script using eqs. 15-17:

$$P_{ij} = \frac{s_i s_j}{2m}, [\mathbf{15}]$$

where

$$s_i = \sum_j A_{ij}, [\mathbf{16}]$$

and

$$m = \frac{1}{2}\sum_{ij} A_{ij}. [\mathbf{17}]$$

where $\boldsymbol{s_i}$ is the strength of node i, the sum of all its weights to other nodes.

The modularity quality function was maximized using a Louvain-like community detection algorithm. Briefly, the Louvain algorithm is a greedy optimization algorithm wherein each node starts in its own community, node community assignment is changed locally, and changes that increase modularity are kept until there are no further increases in quality (*52, 53*). The Louvain algorithm was iterated until the algorithm converged on the final module assignment. Because the modularity landscape is rough, with many near-optimal solutions (*46*), we assigned a node's module to be the mode of its module assignment over 50 optimizations.

For both single-layer and multilayer networks, γ was tuned separately and manually for spatially and functionally generated graphs to minimize the difference between the number of communities detected for spatial and functional networks. In addition to the value of Q, the Louvain algorithm outputs the partition g, a vector containing the

community number of each node. The Adjusted Rand Index (*ARI*) was used to measure the similarity of community partitions. It is defined mathematically as:

$$ARI = \frac{\binom{N}{2}(a+f) - [(a+b)(a+e) + (e+f)(b+f)]}{\binom{N}{2}^2 - [(a+b)(a+e) + (e+f)(b+f)]}, [\mathbf{18}]$$

where N is the total number of nodes, a is the number of pairs of nodes that are in the same community in the functional partition, g_f, and the spatial partition, g_s, b is the number of pairs of nodes that are in a different community in g_f and g_s, e is the number of pairs of nodes that are in the same subset in g_f and a different subset in g_s, and f is the number of pairs of nodes that are in a different subset in $g_f$and the same subset in g_s. For astrocytes, *ARI* was also calculated for g_a, the actual partitioning of astrocyte segments into cells, versus g_f and g_s. *ARI* can be negative, indicating that the partitions disagree more than what would be predicted by chance, and has a maximum of one for total agreement.

Supplementary Figures

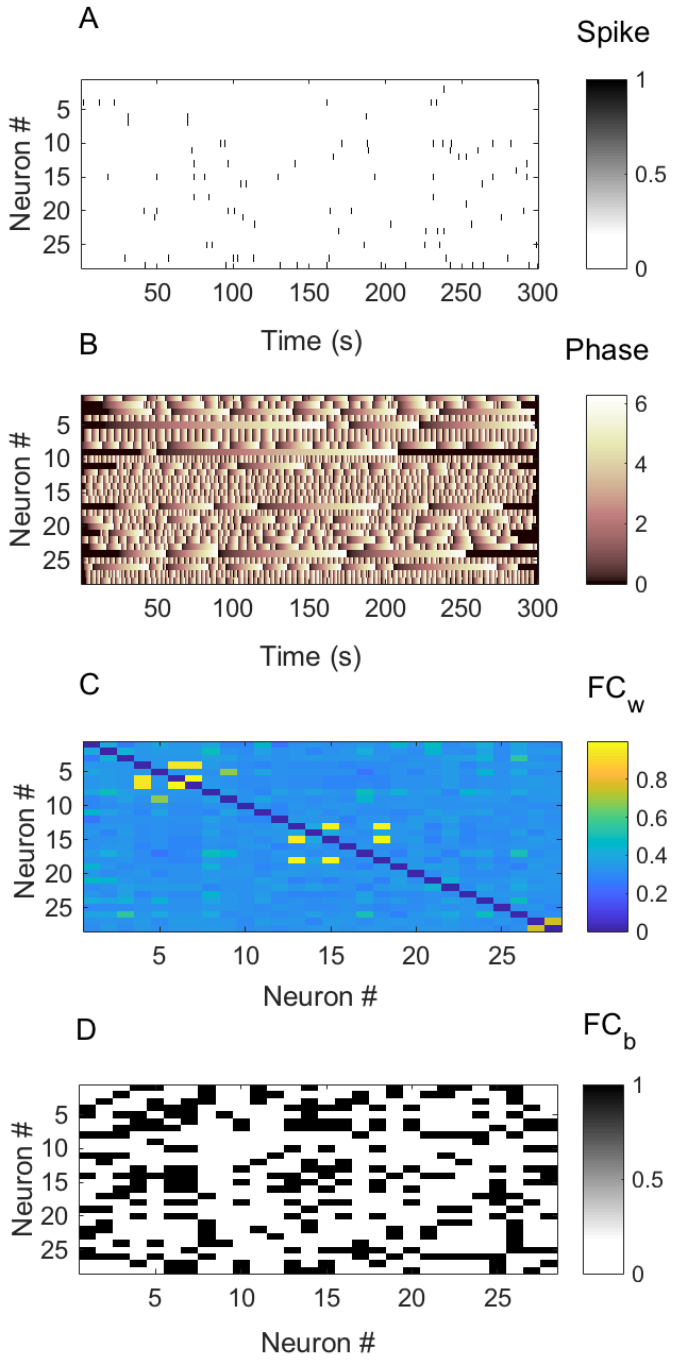

Fig. S1. Example conversion of spike train to neuronal adjacency matrices for a single dish. (**A**) Raster plot showing the spike trains (binary events over time) for each

neuron in the network. (**B**) Instantaneous phase of each neuron over time. (**C**) Weighted adjacency matrix calculated using circular variance of the absolute phase difference between all pairs of neurons. (**D**) Binary adjacency matrix calculated by comparing the absolute phase difference between all pairs of neurons to a surrogate time series and assigning weights only to pairs with a statistically significantly different phase difference.

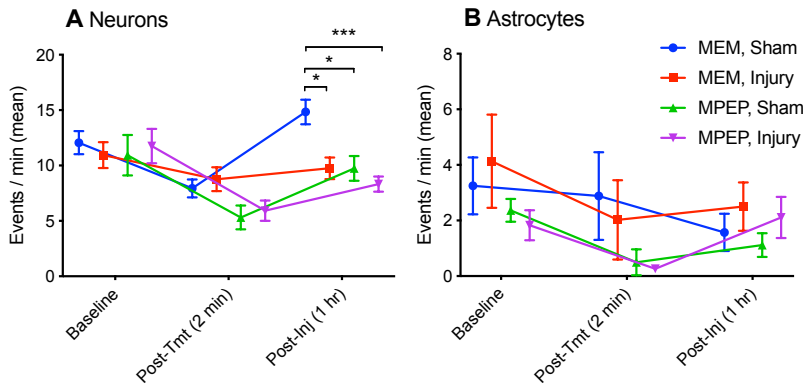

Fig. S2. mGluR$_5$ inhibition and injury decrease neuronal but not astrocytic activity level. (**A**) Neuronal event rate (events/min) at the three measured time points for all four treatment groups (n = 9 for MEM/Sham and MEM/Inj, n = 8 for MPEP/Sham, n = 10 for MPEP/Inj). Event rate decreased following treatment with MPEP at the second time point (Post-Tmt) and for injured groups at the third time point (Post-Inj). Differences due to condition (two-way ANOVA, $F(2,64) = 3.081$, $p = 0.0412$), time (two-way ANOVA, $F(2,64) = 22.40$, $p < 0.0001$) and their interaction (two-way ANOVA, $F(6,64) = 2.738$, $p = 0.0197$) were significant. Further, differences between MEM/Sham and MPEP/Injury (Tukey's multiple comparisons test, $q = 5.869$, $df = 96$, $p = 0.0004$), MEM/Sham and MEM/Inj (Tukey's multiple comparisons test, $q = 4.470$, $df = 96$, $p = 0.0111$), and MEM/Sham and MPEP/Sham (Tukey's multiple comparisons test, $q = 4.345$, $df = 96$, $p = 0.0145$) at the third time point were statistically significant. (**B**) Astrocytic event rate (events/min) at the three measured time points. There was no significant difference between groups at any time point. Error bars indicate standard error of the mean (SEM) and asterisks indicate statistical significance. Tmt: treatment; MEM: treated with minimum essential media; MPEP: treated with anti-mGluR$_5$; Injury: subjected to targeted neuronal tap injury; Sham: negative injury control.

	C			*B*			*E*		
	β	t	p	β	t	p	β	t	p
Intercept	0.051	1.362	0.183	0.380*	2.944	0.006	0.023	1.123	0.270
Density	2.346*	9.735	0.000	3.175*	3.847	0.001	2.198*	16.865	0.000
MPEP	0.010	0.306	0.762	-0.218	-1.999	0.055	-0.031	-1.789	0.083
Injury	0.038	1.175	0.249	-0.250*	-2.275	0.030	-0.027	-1.528	0.137
MPEP + Inj	-0.044	-1.057	0.299	0.164	1.139	0.264	0.027	1.183	0.246

Table S1. Results of a generalized linear regression to predict the effect of group assignment on mean clustering coefficient (*C*), mean normalized betweenness centrality (*B*), and global efficiency (*E*) for neuronal networks. The results statistics are reported as follows: β, estimated coefficient; *t*, value of the test statistic for the coefficient; the value of the estimate divided by the standard error of the estimate; *p*, *p*-value for coefficient resulting from a t-test, pr($t > z$), and $df = 31$. The t-test evaluates the null hypothesis that the coefficient for that covariate is equal to zero. Density was a stronger correlate of *C*, *B*, and *E* in control neural networks than in networks extracted from treatment conditions, as evidenced by higher coefficient estimates and statistical significance ($p \leq 0.001$ for all). Treatment condition was not a statistically significant predictor of *C*, *B*, and *E* after controlling for density, except for the injury condition on *B* (t-test on generalized linear regression coefficients, $\beta = -0.250$, $t = -2.275$, $df = 31$, $p = 0.030$). MPEP: treated with anti-$mGluR_5$; Injury: subjected to targeted neuronal tap injury.

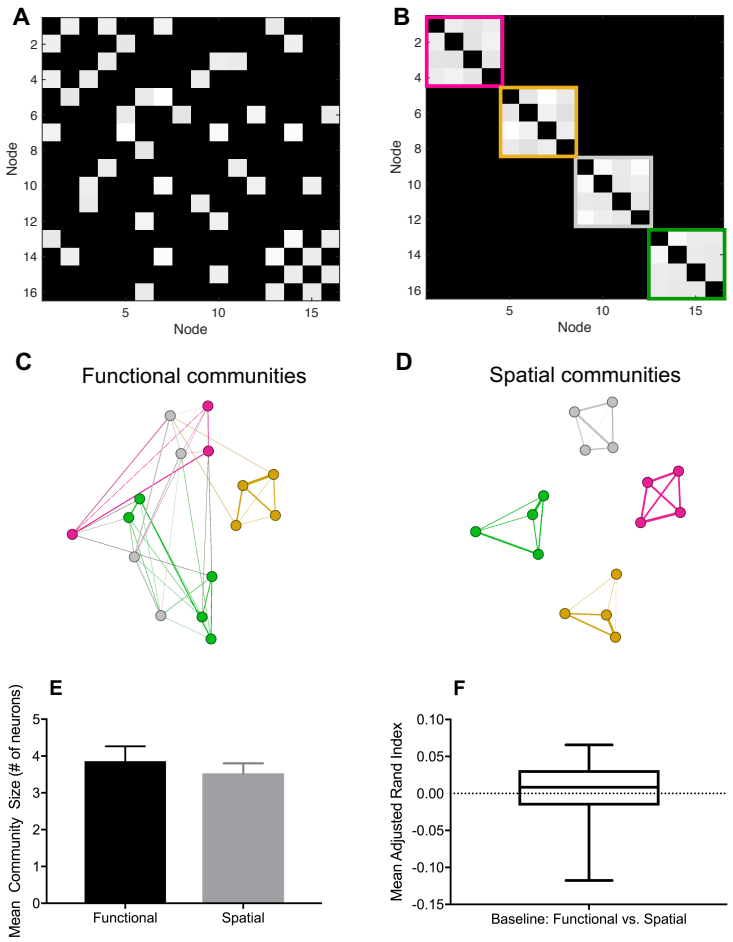

Fig. S3. Community structure of *in vitro* neuronal networks. (**A**) Representative adjacency matrix of a neuronal network. (**B**) The same adjacency matrix shown in panel a after community detection, reordered with modules grouped along the diagonal. (**C**) Graph of the network shown in panel (**A**) and panel (**B**) depicting modularity as determined by functional connectivity between nodes. Nodes of the same color belong to the same functional community. (**D**) Graph of the network shown in panel (**A**) and panel (**B**) depicting modularity as determined by spatial proximity between nodes. Nodes of the same color belong to the same spatial community. If functional connectivity were based on spatial proximity, the modules in panels (**C**) and (**D**) would be the same or similar. However, we did not observe this to be the case, suggesting that functional connectivity is not well-explained by spatial proximity. (**E**) Mean community size does not differ between functional and spatial communities, despite the fact that the spatial tuning

parameter was optimized to minimize this difference (paired t-test, $t = 0.7091$, $df = 35$, $p = 0.4830$). (**F**) Mean Adjusted Rand Index for functionally- versus spatially-generated networks. The mean (0.0021) was not significantly different from zero (two-sided one-sample t-test, $t = 0.3017$, $df = 35$, $p = 0.7647$). Whiskers range from the minimum value to the maximum value.

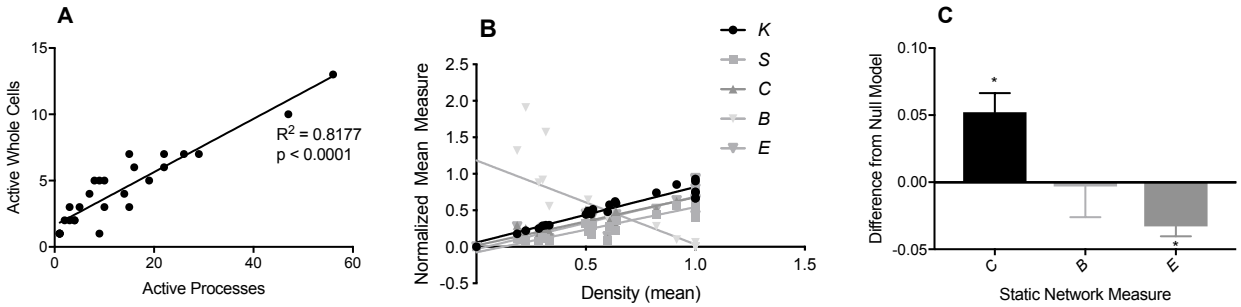

Fig. S4. Astrocyte functional network topology. (**A**) Number of active astrocytes versus number of active processes (n = 27 dishes with at least one active astrocyte). As expected, there is a positive correlation between these two variables (linear regression, R^2 = 0.8643, $F(1,25) = 159.3$, $p \leq 0.0001$), with each active whole cell having around five active processes on average. (**B**) Mean normalized betweenness centrality B, global efficiency E, clustering coefficient C, normalized degree K, and normalized strength S versus density for each dish at the third time point. We observe clear positive correlations between graph statistics and density (for K, R^2 = 0.9183, F(1,21) = 236.0; for S, R^2 = 0.7869, F(1,21) = 77.57; for C, R^2 = 0.6990, $F(1,21) = 48.76$; for B, R^2 = 0.4619, $F(1,21)$ = 18.03; for E, R^2 = 0.7440, $F(1,21) = 61.03$; note that $p < 0.0004$ for all). (**C**) Differences in the clustering coefficient C, normalized betweenness centrality B, and global efficiency E from that of a random network null model with preserved degree distribution and density. The differences in the clustering coefficient C (one-sample t-test on differences between actual values and null values, $t = 3.692$, $df = 22$, $p = 0.0016$) and the global efficiency E (one-sample t-test on differences between actual values and null values, $t = 4.450$, $df = 22$, $p = 0.0002$) were statistically significant.

	C			*B*			*E*		
	β	t	p	β	t	p	β	t	p
Intercept	0.137*	3.866	0.001	1.100*	6.499	0.000	0.093*	2.544	0.021
Strength	1.043*	15.711	0.000	-2.024*	-6.376	0.000	1.128*	16.392	0.000
MPEP	-0.071	-1.777	0.093	-0.201	-1.046	0.310	-0.056	-1.355	0.193
Injury	0.002	0.037	0.971	0.471*	2.440	0.026	-0.009	-0.212	0.835
MPEP + Inj	0.036	0.653	0.523	-0.325	-1.236	0.233	0.033	0.587	0.565

Table S3. Results of generalized linear regression to predict the effect of group assignment on mean clustering coefficient (*C*), mean normalized betweenness centrality (*B*), and global efficiency (*E*) for astrocyte networks. The results statistics are reported as follows: β, estimated coefficient; *t*, value of the test statistic for the coefficient; the value of the estimate divided by the standard error of the estimate; *p*, *p*-value for coefficient resulting from a t-test, pr($t > z$), and $df = 22$. The t-test evaluates the null hypothesis that the coefficient for that covariate is equal to zero. Mean nodal strength was a stronger correlate of graph statistics (including *C*, *B*, and *E*) in neural networks than treatment condition, as evidenced by higher coefficient estimates and statistical significance ($p \leq 0.0001$ for all). Treatment condition was not a statistically significant predictor of graph statistics (including *C*, *B*, and *E*) after controlling for strength, except for the effect of injury on betweenness centrality ($\beta = 0.471$, two-sided t-test on regression coefficient, $t = 2.440$, $p = 0.026$).

	C			*B*			*E*		
	β	t	p	β	t	p	β	t	p
Intercept	0.070*	5.54	0.000	1.138*	19.64	0.000	0.100*	8.256	0.000
Strength	0.892*	29.29	0.000	-2.226*	-15.98	0.000	0.886*	30.471	0.000
MPEP	0.029	1.82	0.083	0.237*	3.24	0.004	0.016	1.076	0.294
Injury	0.035*	2.22	0.037	0.310*	4.30	0.000	0.012	0.792	0.437
MPEP + Inj	-0.030	-1.38	0.180	-0.447*	-4.54	0.000	-0.003	-0.149	0.883

Table S3. Results of generalized linear regression to predict the effect of group assignment on mean clustering coefficient (*C*), mean normalized betweenness centrality (*B*), and global efficiency (*E*) for multilayer networks. The results statistics are reported as follows: β, estimated coefficient; *t*, value of the test statistic for the coefficient; the value of the estimate divided by the standard error of the estimate; *p*, *p*-value for coefficient resulting from a t-test, pr($t > z$), and $df = 22$. The t-test evaluates the null hypothesis that the coefficient for that covariate is equal to zero. In this case, strength was not the only significant correlate of *B*, as evidenced by $p < 0.05$ for MPEP, Injury, and MPEP + Injury group assignments in these measures. The clustering coefficient *C* was significantly predicted by injury (generalized linear model, effect of injury: $\beta = 0.035$, t = 2.22, $df = 22$, $p = 0.037$). After controlling for changes in strength, the betweenness centrality *B* was significantly predicted by injury, MPEP, and the interaction of injury and MPEP; using a generalized linear model, we observed a statistically significant effect of MPEP ($\beta = 0.237$, $t = 3.24$, $df = 22$, $p = 0.004$), a statistically significant effect of injury ($\beta = 0.310$, $t = 4.30$, $df = 22$, $p = 0.0003$), and a statistically significant interaction ($\beta = -0.447$, $t = -4.54$, $df = 22$, $p = 0.0002$). MPEP: treated with anti-mGluR$_5$; Injury: subjected to targeted neuronal tap injury. Error bars indicate standard error of the mean (SEM) and asterisks indicate statistical significance.

	C			*B*			*E*		
	β	t	p	β	t	p	β	t	p
Intercept	0.046*	3.95	0.001	1.040*	20.41	0.000	0.089*	9.717	0.000
Strength	0.950*	34.72	0.000	-1.879*	-15.74	0.000	0.909*	42.520	0.000
MPEP	0.020	1.33	0.196	0.218*	3.36	0.003	0.011	0.955	0.350
Injury	0.028	1.94	0.066	0.163*	2.60	0.016	0.011	0.983	0.336
MPEP + Inj	-0.006	-0.27	0.789	-0.304*	-3.46	0.002	0.007	0.436	0.667

Table S4. Results of generalized linear regression to predict the effect of group assignment on mean clustering coefficient (*C*), mean normalized betweenness centrality (*B*), and global efficiency (*E*) for weighted neuron networks. The results statistics are reported as follows: β, estimated coefficient; *t*, value of the test statistic for the coefficient; the value of the estimate divided by the standard error of the estimate; *p*, *p*-value for coefficient resulting from a t-test, pr($t > z$), and $df = 22$. The t-test evaluates the null hypothesis that the coefficient for that covariate is equal to zero. Mean nodal strength was the strongest predictor of C, B, and E, as evidenced by p _ 0.0001 for all coefficients. In this case, only changes in the betweenness centrality B were significantly predicted by treatment condition (generalized linear model, effect of MPEP: $\beta = 0.218$, $t = 3.50$, $df = 22$, $p = 0.002$; injury: $\beta = 0.163$, $t = 2.60$, $df = 22$, p = 0.016; MPEP + injury: $\beta = -0.304$, $t = -3.46$, $df = 22$, $p = 0.002$).

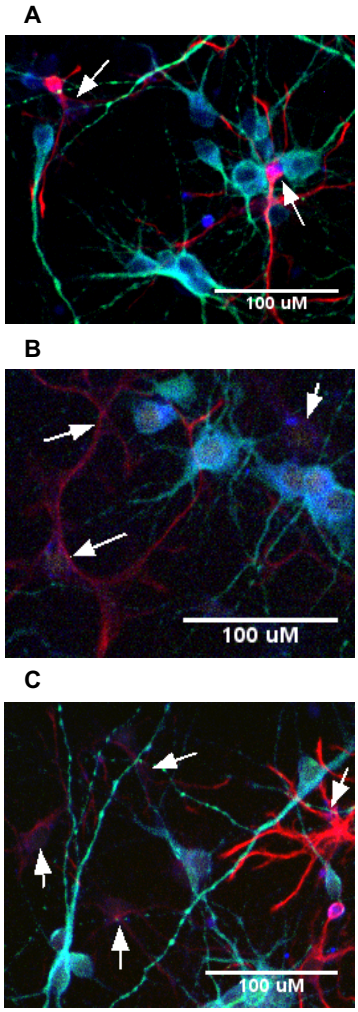

Fig. S5. Immunofluorescent staining confirms expression of mGluR$_5$ in neurons and astrocytes. Cells were stained for GFAP (red), an astrocytic marker, MAP2 (green), a neuronal marker, and mGluR$_5$ (blue). Turquoise and magenta areas represent co-localization of mGluR$_5$ on neurons and astrocytes, respectively. Shown in panels (**A**) – (**C**) are cropped fields of view from three dishes. Astrocytes expressing mGluR$_5$ are indicated with white arrows.

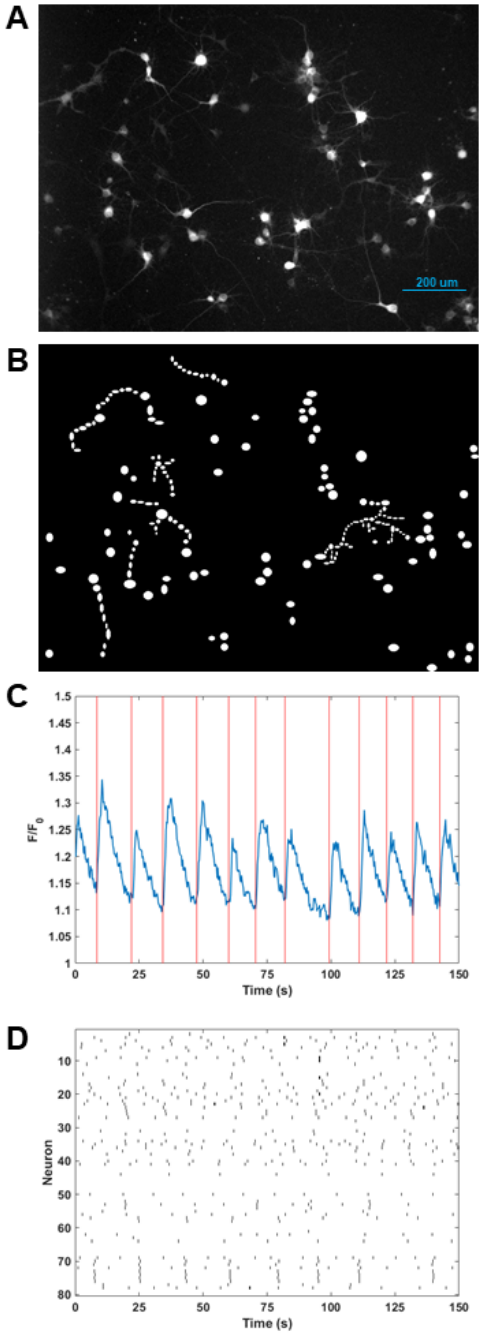

Fig. S6. *In vitro* calcium image acquisition and processing of neuron-astrocyte networks. (**A**) Maximum fluorescence projection of the video recording. (**B**) Manually identified ROIs segmenting neurons and astrocyte segments. (**C**) Scaled fluorescence trace for a single neuronal ROI. (**D**) Raster plot (spikes over time) of all neuronal ROIs in the field of view.